Max-Planck-Institut
für Meteorologie

REPORT No. 68

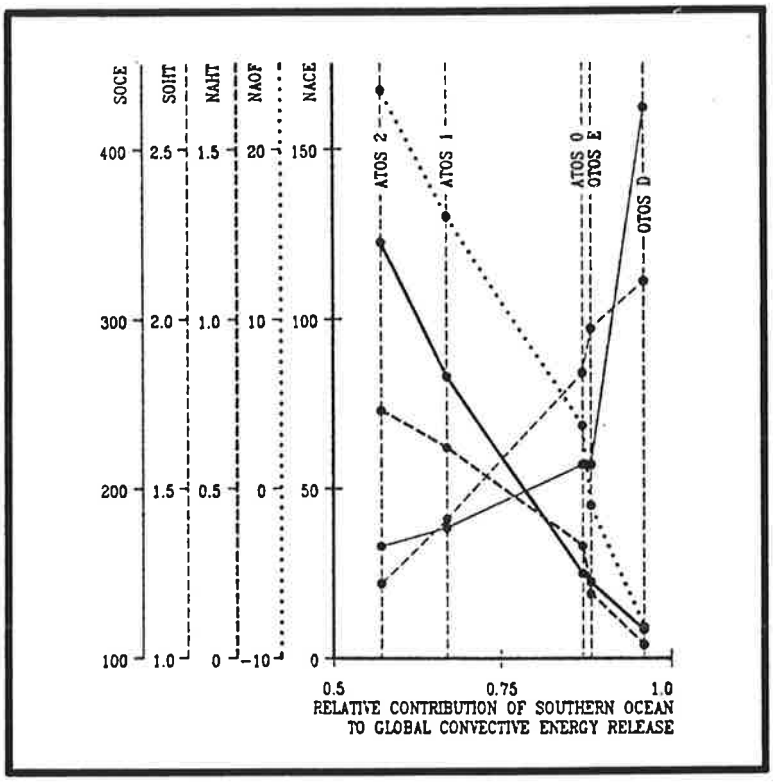

ON THE SENSITIVITY OF THE GLOBAL OCEAN CIRCULATION TO CHANGES IN THE SURFACE HEAT FLUX FORCING

by

ERNST MAIER-REIMER • UWE MIKOLAJEWICZ
KLAUS HASSELMANN

HAMBURG, JULY 1991

AUTHORS:

ERNST MAIER-REIMER

UWE MIKOLAJEWICZ

KLAUS HASSELMANN

MAX-PLANCK-INSTITUT
FUER METEOROLOGIE

MAX-PLANCK-INSTITUT
FUER METEOROLOGIE
BUNDESSTRASSE 55
D-2000 HAMBURG 13
F.R. GERMANY

Tel.: (040) 4 11 73-0
Telex: 211092 mpime d
Telemail: MPI.METEOROLOGY
Telefax: (040) 4 11 73-298

REPb68

ON THE SENSITIVITY OF THE GLOBAL OCEAN CIRCULATION TO CHANGES IN THE SURFACE HEAT FLUX FORCING

Ernst Maier-Reimer
Uwe Mikolajewicz
Klaus Hasselmann

Max Planck-Institut für Meteorologie
Bundesstr.55, 2 Hamburg 13, FRG

ABSTRACT

The sensivity of the global ocean circulation to changes in surface heat flux forcing is studied using the Hamburg Large Scale Geostrophic (LSG) ocean circulation model. The simulated mean ocean circulation for optimally tuned surface forcing fields reproduces the principal water mass properties, residence times and large scale transport properties of the observed ocean circulation quite satisfactorily. However, rather minor changes in the formulation of the high latitude air - sea heat flux can produce dramatic changes in the structure of the ocean circulation. These strongly affect the deep ocean overturning rates and residence times, the oceanic heat transport and the rate of oceanic uptake of CO_2. The sensivity is largely controlled by the mechanism of deep water formation in high latitudes. The experiments support similar findings by other authors on the sensivity of the ocean circulation to changes in the fresh water flux and are consistent with the existence of multi-equilibria circulation states with a relatively low transition threshold.

1. INTRODUCTION

The oceans play a major role in the dynamics of climate through their large capacity for the transport and storage of heat, moisture and CO2. The oceans are driven by the atmosphere, and their response to changes in atmospheric forcing represents one of the most important coupling links within the complex system of climatic feedbacks. The ocean - atmosphere coupling has a strong impact both on the response

ISSN 0937-1060

characteristics of the climate system to external forcing and on internal natural climatic variability.

In addition to these general considerations, there is mounting evidence that the global ocean circulation is a highly sensitive component of the climate system which can be rather easily driven from one circulation regime to another. The suggestion that the global ocean circulation may exhibit more than one distinct mode of circulation has long been the subject of speculation. Geological evidence indicates that during some periods in the Tertiary, the deep ocean was some ten degrees warmer and more saline than today, suggesting that in those times deep water was formed by an evaporation-salinity pump operating at relatively low latitudes, e.g. in the Mediterranean, rather than by cooling and freezing in high latitudes, as in today's ocean. Stommel (1962) and Rooth (1982) have suggested that even for the same boundary conditions, the ocean circulation may have two distinct steady state solutions. This conjecture has been supported by numerical experiments with an ocean general circulation model (OGCM) with idealized geometry by Bryan (1986) and by coupled ocean-atmosphere general circulation model experiments by Manabe and Stouffer (1989). The mechanism of such multiple equilibrium states has been investigated in more detail by Welander (1986) and Marotzke et al. (1987).

The sensitivity of the ocean circulation as evidenced by multi-equilibria states is bourne out also by the strong response of the ocean circulation to small changes in external forcing. It has been conjectured, for example, by Berger and Killingley (1982) and Broecker et al (1988) that the sudden return of glacial conditions during the Younger Dryas interruption of the holocene warming was due to a transition in the ocean circulation regime triggered by the melt water run-off from the Laurentide ice sheet. This hypothesis has found support through numerical experiments with the Hamburg ocean general circulation model (Maier-Reimer and Mikolajewicz, 1989). Although advanced techniques of dating now seem to rule out the meltwater hypothesis as an explanation specifically of the Younger Dryas (Berger, 1990), Sarnthein and Tiedemann (1990) have recently identified several cooling events within the last glacial cycle which appear consistent with the meltwater mechanism.

Smaller climatic fluctuations, such as the warming around 1000 aD and the little ice age between the 16^{th} and 18^{th} century, may also have been caused by internal variations of the coupled global ocean-atmosphere circulation system. This view has found support in numerical experiments in which an OGCM was driven by white noise atmospheric forcing (Mikolajewicz and Maier-Reimer, 1990).

Further interest in the stability of the ocean circulation has been stimulated by the recent discovery of significant variations in past atmospheric CO_2 concentrations inferred from the analysis of air bubbles trapped in ice cores. A strong correlation has been found between these variations and the observed climate change during the last 160,000 years (Jouzel et al, 1987). Since the oceans represent by far the largest active carbon reservoir in the carbon cycle, most attempts to explain these observations have hypothesized some mechanism for changing the carbon stored in the ocean (cf. review by Berger, 1984). An obvious possible mechanism is the change in the ocean biological pump and deep ocean carbon storage resulting from a change in the ocean circulation. Recent numerical experiments using a global carbon cycle based on the Hamburg global ocean circulation model (Maier-Reimer and Hasselmann, 1987, Bacastow and Maier-Reimer, 1990) indicate that this process is indeed a promising candidate for explaining most, although probably not all, of the observed changes in the carbon system during the last 160,000 years (Heinze et al, 1991, Heinze and Hasselmann, 1991). The effectivity of the process, however, again depends critically on the sensitivity of the ocean circulation to changes in the surface forcing associated with the assumed climatic variations.

In this paper we use the Hamburg LSG global ocean circulation model to investigate the response of the ocean circulation to various modifications in the mean annual (climatological) surface forcing. The ocean circulation is computed for a number of alternative formulations of the surface boundary conditions. All of these may be regarded as acceptable representations of present climatological surface conditions, within the uncertainty of the observations, yet the differences in the simulated circulation patterns are dramatic, particularly in the abyssal ocean. The main source of this sensitivity lies in the formation of deep

water at high latitudes, which depends critically on the heat exchange with the atmosphere.

The Hamburg LSG model does not resolve eddies. Reservations have frequently been expressed regarding the applicability of non-eddy resolving ocean circulation models. We believe these reservations have sometimes been exaggerated. Since their inception in the late sixties, global ocean circulation models have been reasonably successful in reproducing many of the qualitative features of the global ocean circulation (Bryan, 1968, Bryan and Lewis, 1979). Moreover, inversion methods based on essentially the same non-eddy resolving physics as these models have been successfully applied to reconstruct realistic velocity fields from hydrographic and tracer data (Roemmich and Wunsch, 1985, Olbers et al, 1985).

The early global ocean circulation models nevertheless suffered from certain basic shortcomings, such as a too deep main thermocline (typically by a factor of order two) and a slow warming of the deep ocean. These have tended to restrict the application of the models in the fully prognostic thermodynamics mode, leading for example to the introduction of the semi-prognostic "robust diagnostic" technique for long integrations (Sarmiento and Bryan, 1982). However, most of these shortcomings have been largely overcome today through the use of improved numerical methods and a more realistic treatment of diffusion (Redi, 1982). Apart from the western boundary currents and their immediate recirculation regimes (which cannot be adequately resolved by present global ocean models, independent of the role of eddies in these regions), the principal features of the observed global ocean circulation, including the main thermocline and deep ocean circulation, are reproduced remarkably well by, for example, the Hamburg non-eddy resolving global circulation model.

The version of the model used in this paper has 11 vertical layers and a horizontal resolution of 3.5° x 3.5° on an E grid, with realistic bottom topography and coastlines. An implicit time integration method is used, permitting a long time step of one month. The model has been applied recently in a number of ocean circulation studies (cf. Mikolajewicz et al, 1990, Maier-Reimer et al., 1990a) and has been

coupled with the Hamburg atmospheric climate model (Bakan et al., 1991, and Cubasch et al., 1991) . It has also provided the circulation field for the Hamburg carbon cycle model (Heinze and Maier-Reimer, 1990; Maier-Reimer and Bacastow, 1990, and other papers cited above).

A general description of the model (which has not been presented in detail in these previous papers) is given in Section 2. Further technical details can be found in the appendices (on mode decomposition, mode dispersion properties and numerical diffusion) and in Maier-Reimer and Mikolajewicz (1990). Section 3 describes the mean ocean circulation of the "standard" run. This corresponds to a choice of climatological surface boundary conditions which yielded the closest agreement with the observed circulation. The general structure of the simulated ocean circulation is analyzed with respect to currents, transports and water mass properties, including apparent age, surface origin of deep waters and tracer concentrations. The ocean circulation solutions obtained with alternative formulations of the climatological surface boundary conditions are presented in Section 4. The last Section 5 summarizes the principal conclusions of the paper

2 . THE GLOBAL OCEAN CIRCULATION MODEL

The Hamburg Large Scale Geostrophic ocean circulation model has evolved from an original concept of Hasselmann (1982). This was based on the observation that for a large scale ocean circulation model designed for climate studies, the relevant characteristic spatial scales are large compared with the internal Rossby radius throughout most of the ocean, while the characteristic time scales are large compared with the periods of gravity modes and barotropic Rossby wave modes. Under these scaling conditions, the baroclinic velocity field can be determined diagnostically from the given density field through local geostrophy. The barotropic velocity field and surface elevation can also be determined diagnostically for a given density field as the equilibrium barotropic response to the prescribed surface stress forcing and bottom torque. The

only prognostic equations are thus the remaining advection equations for temperature and salinity (for a linearized equation of state, these are identical in the assumed scaling limit to the potential vorticity equation). The approximation breaks down at the equator and in boundary current regions, where it was proposed that the global model should be coupled with appropriate regional models.

By filtering out in this manner the irrelevant fast modes, retaining only the slow modes represented by the prognostic temperature and salinity equations, Hasselmann estimated that a relatively long time step of one month could be achieved, as compared with a few hours for explicit primitive equation models. However, it was found in practice that a straightforward numerical implementation of these concepts led to various numerical instability problems due to numerically induced mode mixing, particularly in the treatment of the interactions with the bottom topography.

Accordingly, in the present version of the model, the fast modes have been filtered out by the more conventional technique of integrating the complete set of primitive equations, including all terms except the nonlinear advection of momentum, by an implicit time integration method. The free surface is also treated prognostically, without invoking a rigid lid approximation. The numerical scheme is unconditionally stable and has the additional advantage that it can be applied uniformly to the entire globe, including the equatorial and coastal current regions. The simulations presented in this paper were carried out with a one month time step.

Applying the standard hydrostatic and the Boussinesq approximations and neglecting the vertical friction, the prognostic equations of the system (in standard notation) are given by:
the horizontal momentum equation,

$$u_t - 2v\Omega\sin\varphi + \frac{1}{\cos\varphi}\frac{p_\lambda}{\rho_0} = \frac{\tau^\lambda}{\rho_0} + A\,\Delta\,u \qquad (1)$$

$$v_t + 2u\Omega\sin\varphi + \frac{1}{R}\frac{p_\varphi}{\rho_0} = \frac{\tau^\varphi}{\rho_0} + A\,\Delta\,v \qquad ; \qquad (2)$$

the equation for the evolution of the potential temperature ϑ and salinity S (neglecting diffusion terms),

$$\vartheta_t + \frac{u}{R\cos\varphi}\vartheta_\lambda + \frac{v}{R}\vartheta_\varphi + w\vartheta_z = q^\vartheta \qquad (3)$$

$$S_t + \frac{u}{R\cos\varphi}S_\lambda + \frac{v}{R}S_\varphi + w\,S_z = q^S \qquad (4)$$

(the sources q^ϑ and q^S occur only in the surface layer);
and the evolution equation for the surface elevation ζ, given by the surface boundary condition,

$$\zeta_t = w \text{ at } z = 0. \qquad (5)$$

The prognostic equations are complemented by the diagnostic relations, consisting of:

the equation of continuity,

$$w_z + \frac{1}{R}\left((v\cos\varphi)_\varphi + \frac{u_\lambda}{\cos\varphi} \right) = 0; \qquad (6)$$

the hydrostatic pressure

$$p = g\rho_0\,(\zeta + \frac{1}{\rho_0}\int_0^z \rho(z')dz') \; ; \qquad (7)$$

and the equation of state, for which we use the UNESCO-83 formula,

$$\rho = \rho(S,T,p), \qquad (8)$$

where the in-situ temperature T is expressed as a function of p and the potential temperature ϑ.

It is convenient to decompose the velocities in the form

$$(u,v) = (U + u', V + v') \; , \qquad (9)$$

where $(U,V) = \int_{-B}^{0}(u,v)\,dz \;/\; B$ and (u',v') denote the barotropic and baroclinic components of motion, respectively. The baroclinic system is described by equations for the vertical velocity shear, obtained from the difference between two adjacent levels of computation. This

corresponds to a decomposition of the N-layer baroclinic system into N-1 two-layer systems, which represent our basic computational modes.

For these modes we derive simplified mode equations which have the same structure as for the barotropic mode:

$$u_t - f\,v + p_x = A\,\Delta u$$

$$v_t + f\,u + p_y = A\,\Delta v \qquad (10)$$

$$p_t + c^2(u_x + v_y) = 0,$$

where c^2 arises through the integration over the stratification. The systems are solved by a rigorous Euler-backward method:

$$u^t - f\,\delta t\,v^t + \delta t p_x^t - \delta t\,A\,\Delta u^t = u^{t-\delta t} \qquad (11a)$$

$$v^t + f\,\delta t\,u^t + \delta t p_y^t - \delta t\,A\,\Delta v^t = v^{t-\delta t} \qquad (11b)$$

$$p^t + \delta t\,c^2(u_x^t + v_y^t) = p^{t-\delta t} \qquad (11c)$$

By insertion of (11c) into (11a) and (11b) we obtain a simultaneous elliptic system for u^t and v^t . For the baroclinic modes the system can be easily solved by iteration. For the barotropic system, however, the iterative procedure was found to converge too slowly and a solution by direct elimination was therefore used. The time consuming step of triangularization need be carried out only once (assuming that the basic stratification does not change substantially during the course of the integration).

The advection of temperature and salinity is computed by an upwind discretization method, which is also implicit in time. The inherent numerical diffusivity of upwind schemes is greater than that of centered difference schemes. On the other hand, centered difference schemes need higher explicit diffusion terms in order to suppress negative side lobes. The required additional diffusivity is generally of the same order as the implicit numerical diffusivity of the first order scheme. In practice, we

found that the numerical dispersion of our scheme was tolerable and if anything slightly smaller (as evidenced, for example by the realistic depth of the main thermocline) than the net diffusivity incurred with existing models of comparable resolution using centered difference schemes (e.g Bryan and Lewis, 1979). The numerical diffusivity is noticeable mainly in regions of strong current shears, where it could be argued that it is in fact needed as a parameterization of the non-resolved mixing by baroclinically unstable current fluctuations and eddies.

Convective mixing is introduced whenever the stratification becomes unstable. Stability of a vertically neighbouring pair of grid cells is defined by comparing their potential densities computed at their common interface level. For equally sized grid cells (below 1000m) we assume complete interchange of water properties. Otherwise we assume the maximal stabilisation which is compatible with the conservation of heat and salt. The mixing algorithm is applied successively to all pairs of layers, beginning from the top. This procedure is performed only once per time step, so that the entire water column does not necessarily become completely stable. However, we found experimentally that a repeated mixing cycle would be activated for only 5% of the locations and would release only 1 % additional potential energy. In the case of ice formation, the evicted brine is distributed equally over the top two layers.

The horizontal spatial discretization is on an E-grid (Arakawa and Lamb, 1976). This has some known disadvantages in the representation of short gravity waves, but for the geostrophic modes of interest here it yields simple interpolation-free difference expressions for the relevant spatial derivatives. The E grid is staggered and therefore produces split modes, but mode divergence is suppressed by the viscosity and diffusion terms.

A general analysis of the dispersion properties of the discretization scheme on the globe has not been attempted. However, some of the principal modifications of wave propagation in mid-latitudes and along the equator are discussed in the β-plane approximation in Appendix 2. The discretization scheme has negligible effect on the propagation of

slow internal Rossby waves, in which we are principally interested, but produces a strong damping and retardation of fast free modes, as intended. The quasi-stationary forced fast modes, which we also wish to retain, are similarly not significantly distorted.

For the present application, the model was run on two staggered $5^\circ \times 5^\circ$ global grids with 11 vertical levels, yielding an effective grid resolution of 3.5°. Horizontal velocity, temperature and salinity were specified at the depth levels 25, 75, 150, 250, 450, 1000, 2000, 3000, 4000 and 5000m, (c.f. Fig 1), while vertical velocity and pressure were defined at the intermediate levels. The model includes a realistic smoothed bottom topography.

In this configuration, the model requires approximately 3 seconds per time step on one CRAY 2S processing unit. This is about four times the requirement of a more conventional GCM with explicit discretization schemes (Sterl et al., 1991). However, the large time step of one month more than offsets the disadvantage of the more complex numerics and makes the model an order of magnitude more efficient than an equivalent explicit model.

In all simulations the circulation was driven by a given wind stress field (from Hellerman and Rosenstein, 1983) and the observed surface layer salinity field (from Levitus, 1982). To smooth the response, the observed salinity values were coupled to the top ocean layer through a linear Newtonian relaxation term with a time constant of typically a few months.

The thermal forcing was similarly computed using a simple Newtonian heat flux relation from a prescribed atmospheric or ocean surface temperature field.

In most experiments, a simple thermodynamic ice model was included. Whenever the heat loss to the atmosphere within a time step leads to an ocean temperature below the freezing point T_f, the temperature is held fixed at T_f and the excess heat loss is used to produce sea ice. The heat flux over sea ice can be represented approximately as

$$H = D(T_a - T_f)/h \qquad (3)$$

where h is the ice thickness, D the heat conductivity of ice, and T_a the

atmospheric temperature (Stefan, 1891). The rate of ice formation is then given by

$$\frac{dh}{dt} = -\frac{H}{E}, \tag{4}$$

where E the enthalpy of melting, which can be solved to yield

$$h = \sqrt{2D(T_f - T_a)(t-t_0)/E} \tag{5}$$

where t_0 is the freezing onset time.

The analytical square root expression (5) applies for the first time step in which sea ice is formed. It yields a better description of ice growth in the initial stages than a straightforward linear finite difference relation (note that the time derivative of the ice thickness is initially infinite). It also yields a correct partioning of the heat flux into ocean and ice. A similar difference formula based on the exact integration of equs. (3), (4) is used also if ice is already present at the onset of a time step.

3. THE REFERENCE RUN

For the reference run, the model was driven by the monthly climatological windstress fields from Hellerman and Rosenstein (1983), by the annual mean surface salinity from Levitus (1982) (as in all runs) and by an effective monthly mean air temperature. The Newtonian time constant was taken as 2 months for both salinity and temperature coupling. The prescribed salinity boundary condition was used to compute an equivalent fresh water flux (rather than an equivalent salinity source, since we wish to conserve salt in our model). The fresh water flux yields a small but non-negligible additional mass flux source term which must be included in the computation of sea level.

To determine the effective air temperature, the observed atmospheric surface temperatures from the COADS data set were combined with the climatological windfield in an advection equation

$$T_t + v_1 \partial_1 T = \lambda \, (T_{COADS} - T) \tag{12}$$

Eq. 12 may be regarded as a simple one-layer parameterization of the atmospheric boundary layer. The approach was motivated by the observation that the measured monthly mean atmospheric temperatures, averaged over a grid resolution cell, are normally rather close to thermal equilibrium with the oceans. These climatological mean values are unable to capture the strong heat transfer from the oceans to the atmosphere through short sub-time-scale synoptic processes such as cold air outbreaks from the continents, cold polar air flows in the afterwake of passing cyclones etc. A reliable estimate of these contributions would require a detailed statistical analysis of the correlation of the short time scale fluctuations of air, temperature and windspeed. As this is difficult to carry out on a global basis, we attempt to parameterize such sub-scale processes by the simple ingredient of an advection term proportional to the local mean wind velocity. This has the plausible property that it yields the largest contributions where the background mean wind field crosses strong thermal gradients in the ocean (e.g. off continental coasts and near thermal fronts such as the Gulf Stream). In general, the advection corrections are larger in the northern than in the southern hemisphere, where the wind fields and surface ocean currents tend to be more strongly zonally aligned. As discussed in the following section, the introduction of such a sub-grid scale correction term significantly improved the simulation of North Atlantic deep water formation and the deep ocean circulation in general.

The gross transport properties of the global ocean circulation are summarized in Fig. 1, which shows the integrated net mass fluxes between various characteristic ocean regions. The annual mean circulation was averaged for this representation over 24 boxes, obtained by dividing the ocean into an upper and lower layer, separated by the 1500 m depth level, and segmenting the layers by latitudinal boundaries at 10°N, 10°S, and 40°S (in addition to the natural meridional ocean basin boundaries). The upper and lower panels of Fig. 1 show the meridional mass fluxes of the three major oceans and the zonal circumpolar flux in the Southern Ocean for the upper and lower layers, respectively. The center panel shows the vertical flux across the 1500 m level interconnecting the two layers.

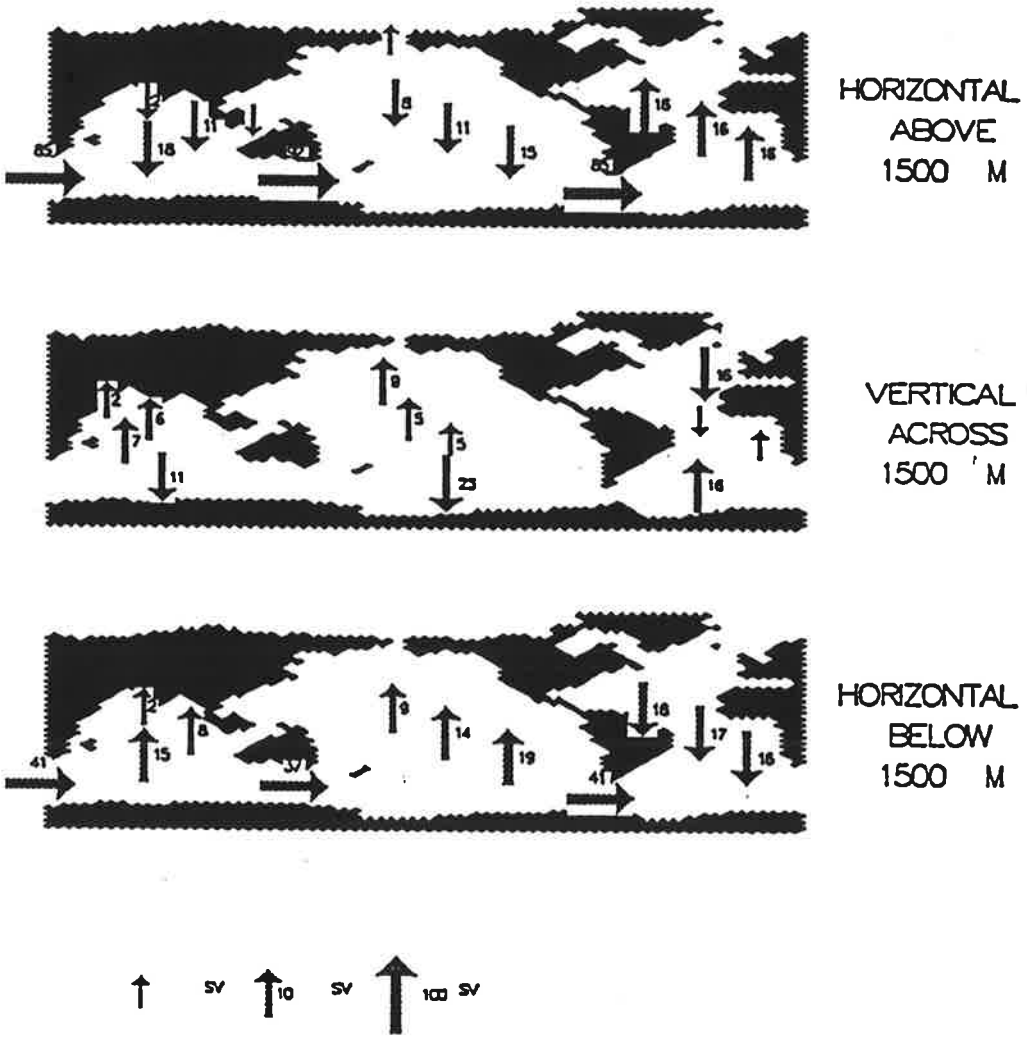

Fig. 1 The conveyor belt circulation of the standard run.

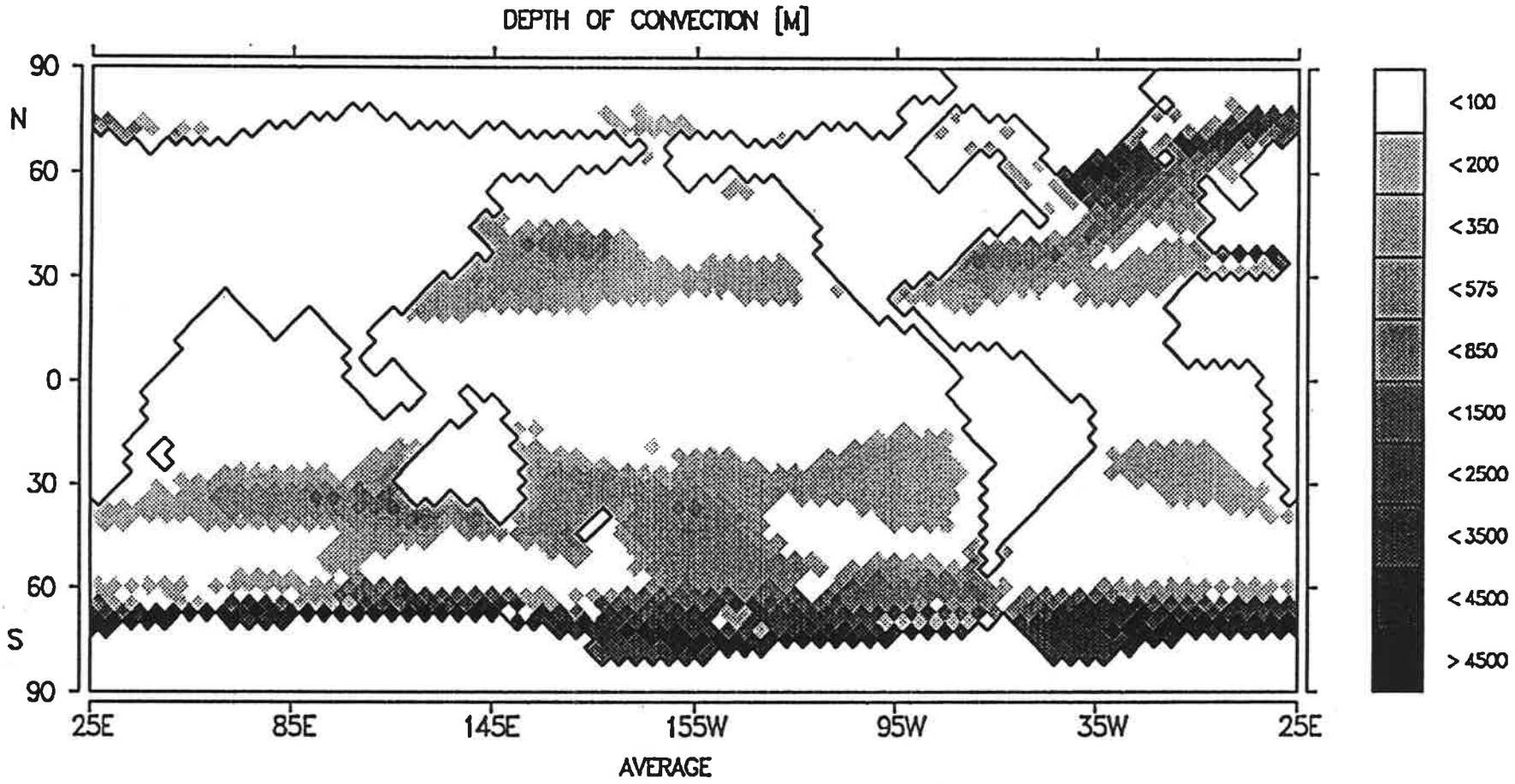

Fig.2a Depth of convective column produced by surface cooling

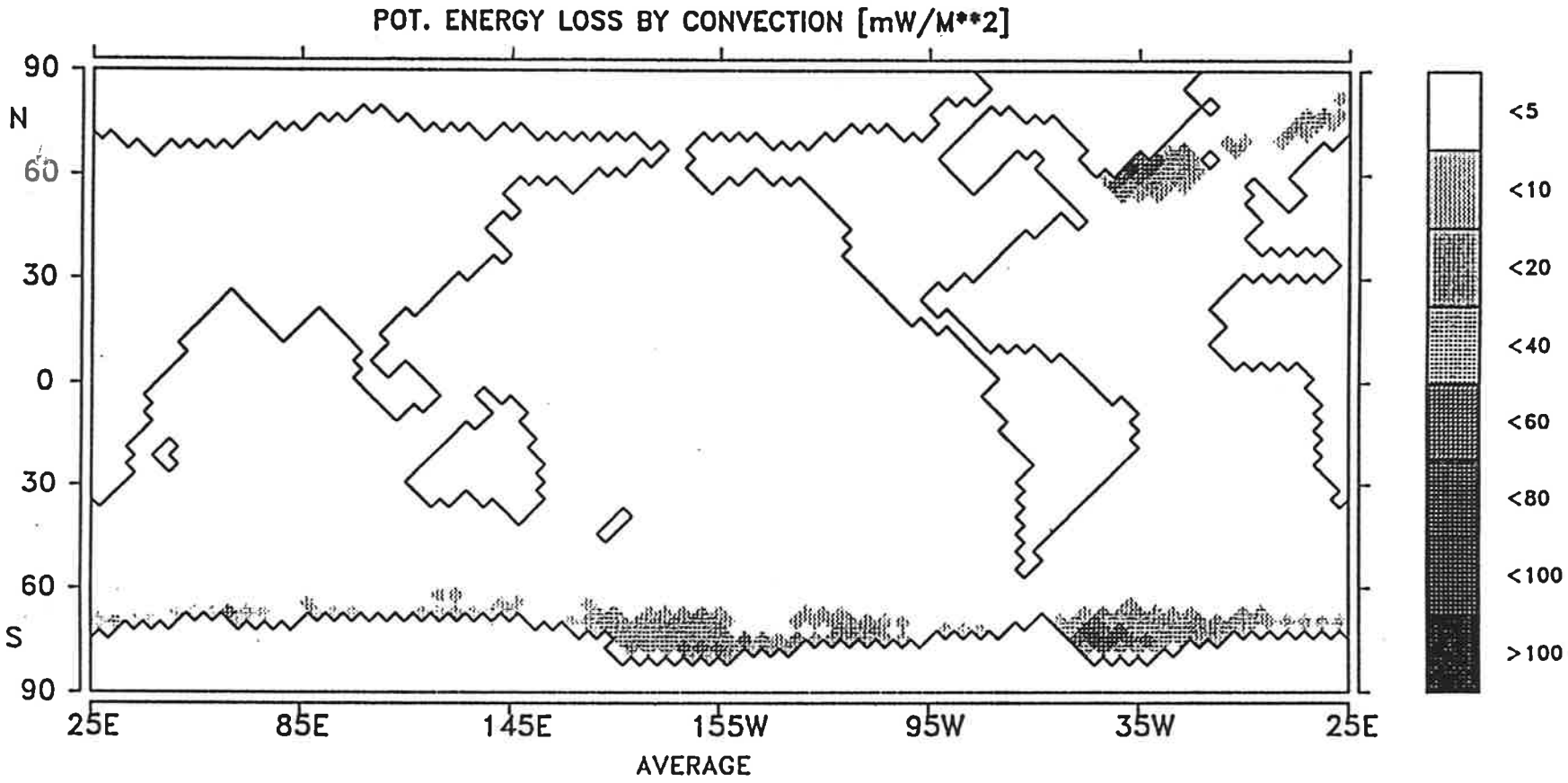

Fig.2b Release of potential energy by convective mixing

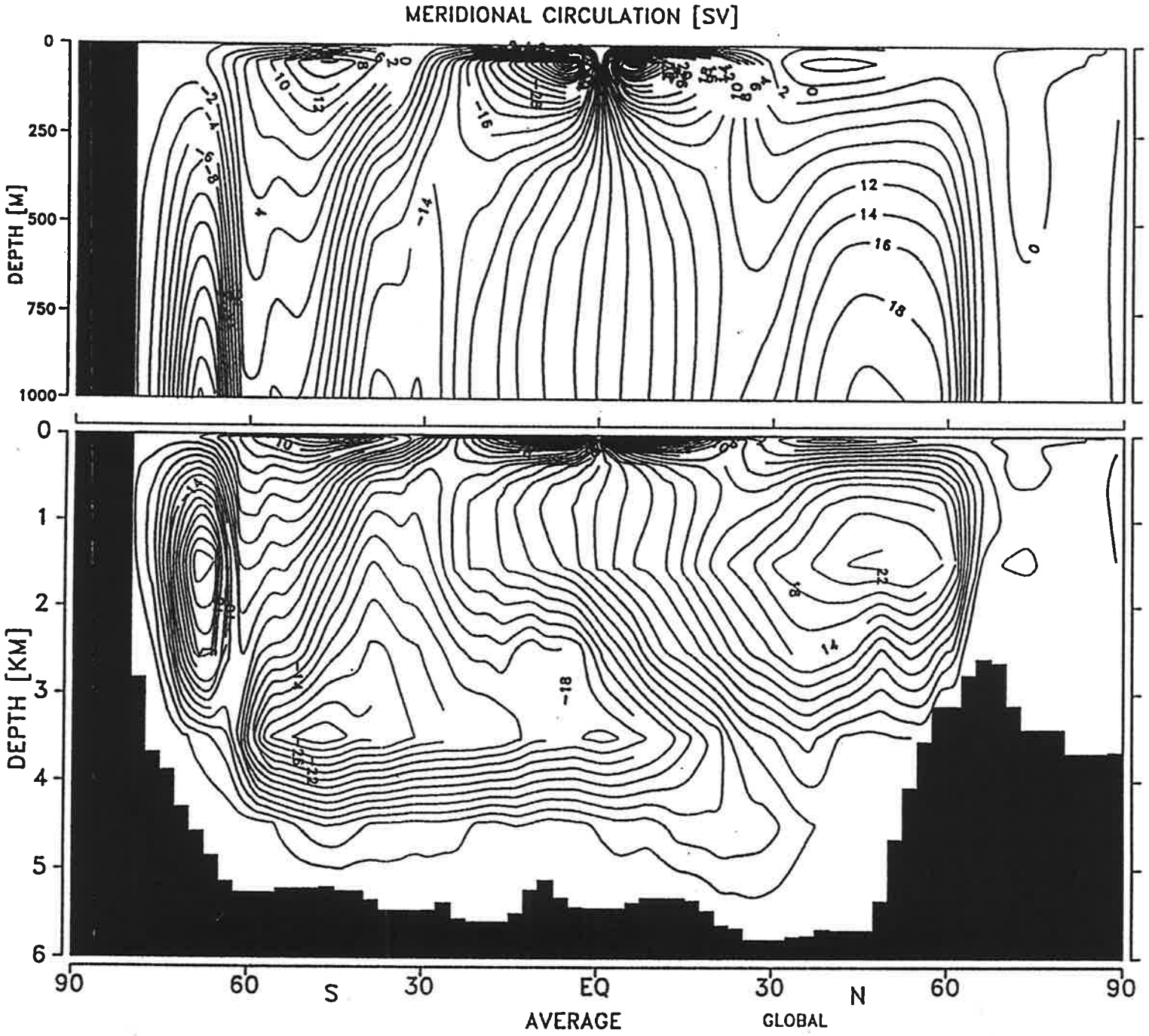

Fig.3a Global meridional overturning circulation

The basic features of the standard "conveyor belt" picture (Wüst, 1938; Gordon, 1985) are well reproduced. The main source of deep water is in the Northern Atlantic. The deep salty water formed first in the Northern Atlantic spreads across the equator into the South Atlantic, Indian Ocean and Pacific, joining the Antarctic circumpolar current. The return flow is almost completely through the Drake passage; only 1.5 Sv pass through the narrow Banda strait between Indonesia and Australia (this feature is very sensitive, however, to the representation of the topography in the Banda strait, which is not well resolved in the present model). Upwelling occurs mainly in equatorial regions.

Fig. 2a shows the depth of the convective column produced by surface cooling (the depth of the convective column is defined as the greatest depth which is connected with the surface by at least one convection event within an annual cycle). Most of the model ocean is seen to be stably stratified. Deep convection occurs mainly around Antarctica, particularly off the Ross- and Weddell shelves, and in the North Atlantic, where two regions of deep water production can be seen: the Irminger Sea, southeast of Greenland, where extremely cold air is advected from the Greenland Ice sheet; and the Norwegian Sea, where high salinity water of the Gulf Stream system extends into the Arctic basin.

Fig. 2a can not be interpreted as a direct measure of the rate of deep water formation, as it contains no information on the strength of convection. A measure of the intensity of convective overturning is provided by the rate of release of potential energy within the water column, shown in Fig. 2b. The North Atlantic and Weddell Sea deep water sources are now more evident. The difference between the North Pacific, characterized by stable stratification, and the convective high latitude regions of the other oceans is also seen more clearly.

Another source of deep water formation is large scale subduction, indicated by the zonally averaged meridional overturning circulation (Fig. 3a). In the surface waters, two nearly symmetrical Ekman cells are formed on either side of the equator, while a third surface cell is seen in the Antarctic Circumpolar Current (ACC). The largest deep overturning cell lies in the Southern Ocean. It is driven mainly by dense Weddell Sea water. However, the overturning cell in the North Atlantic is only

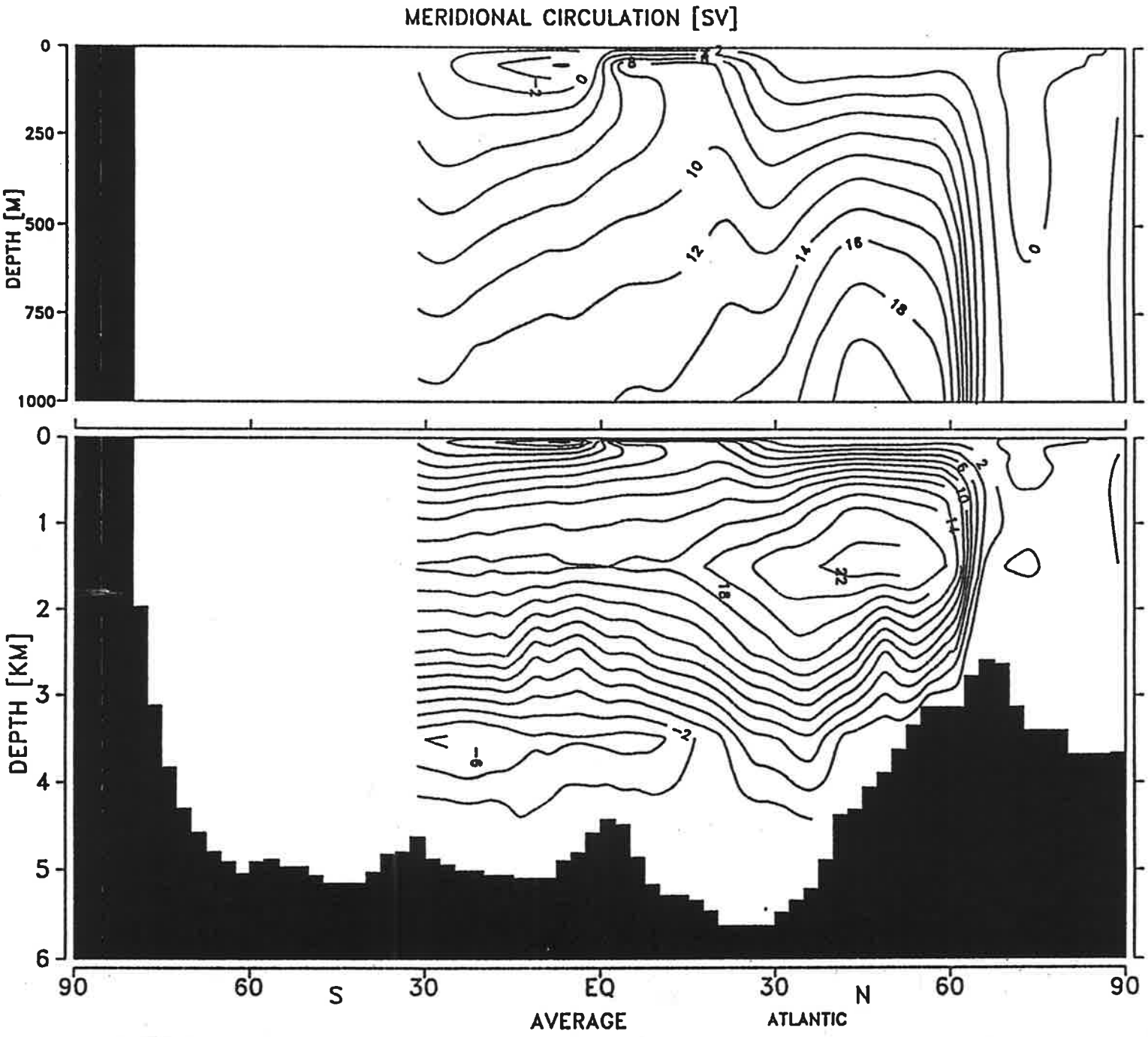

Fig. 3b Atlantic meridional overturning circulation

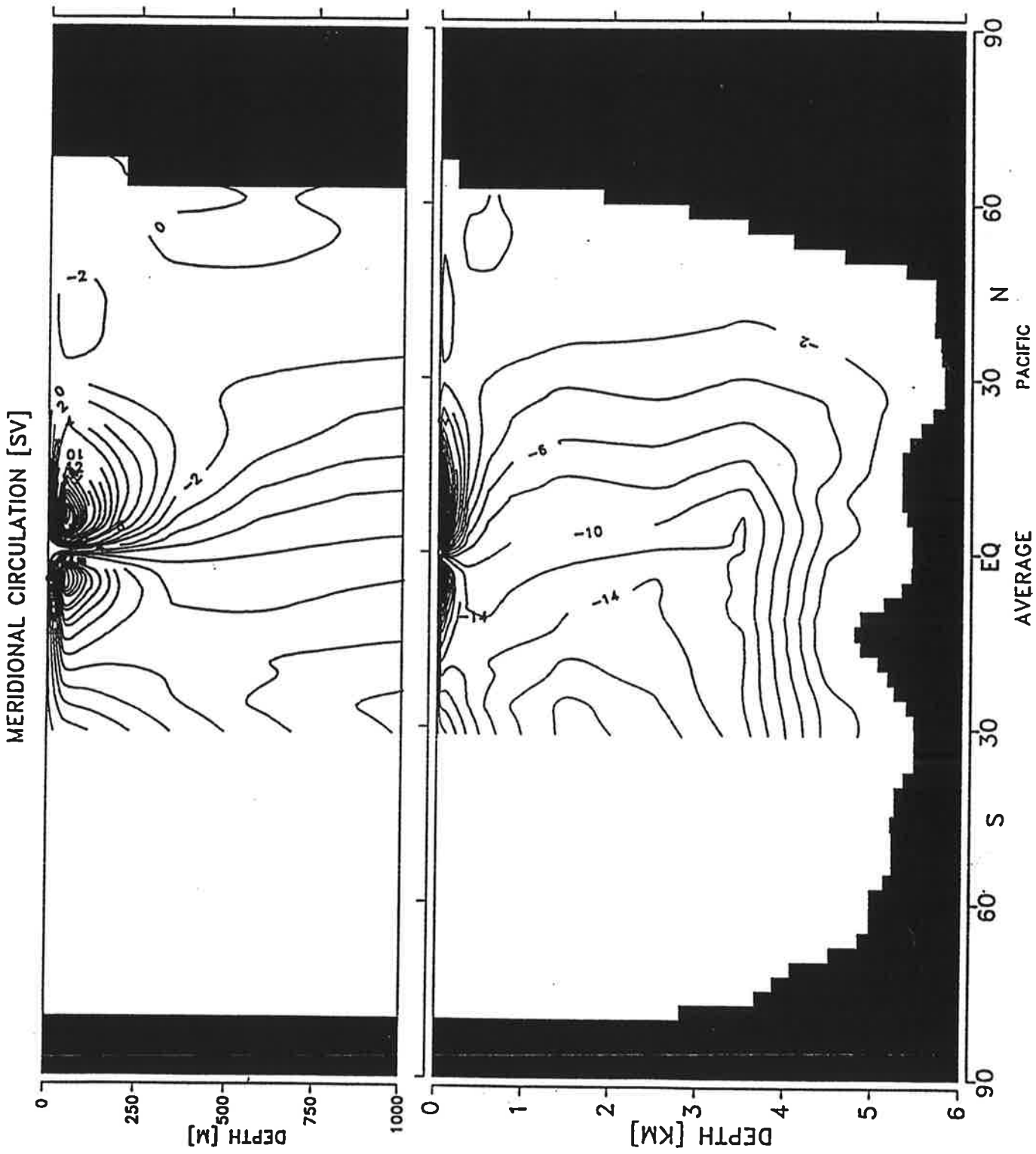

Fig.3c Pacific meridional overturning circulation

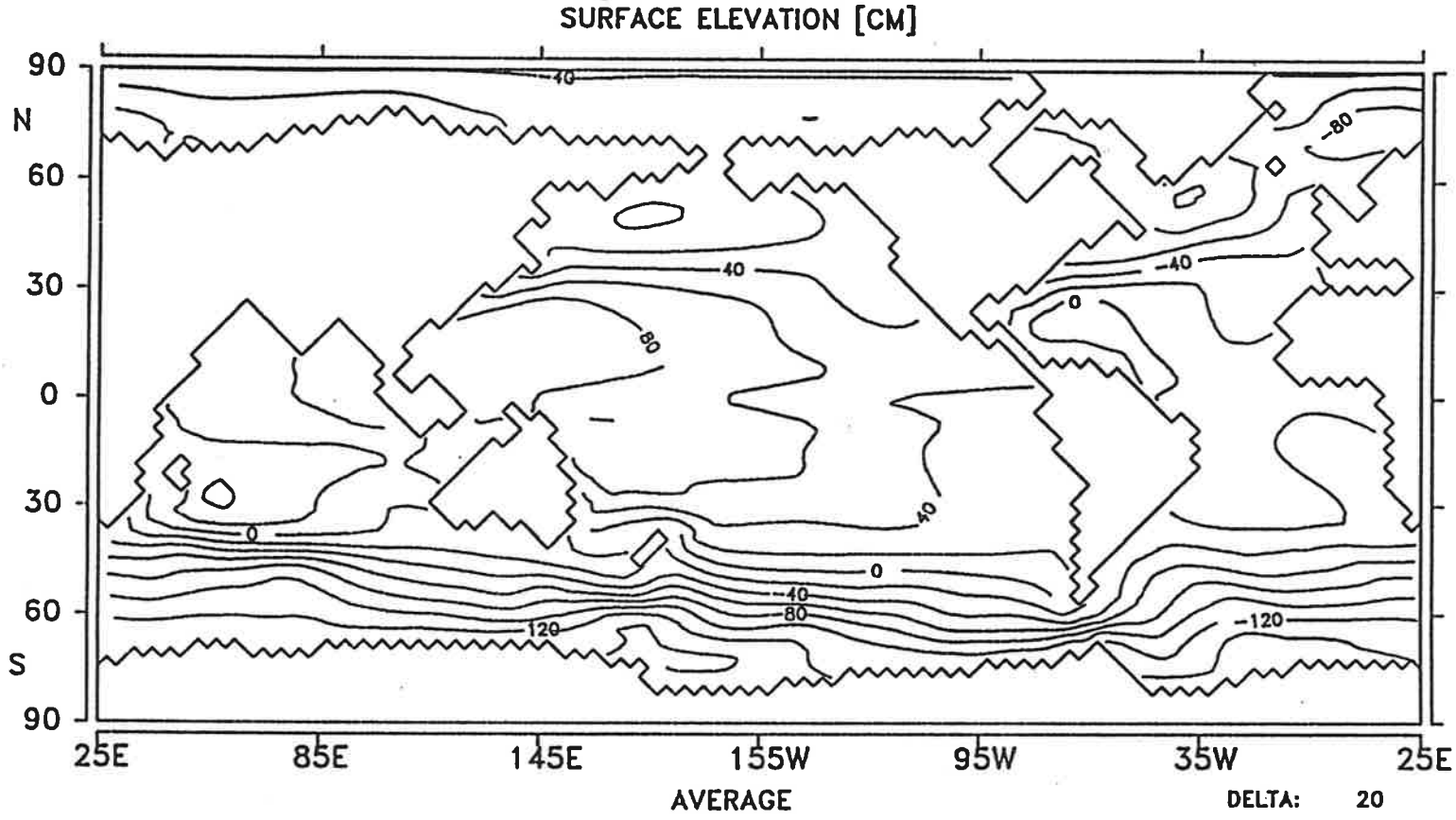

Fig. 4a Surface topography

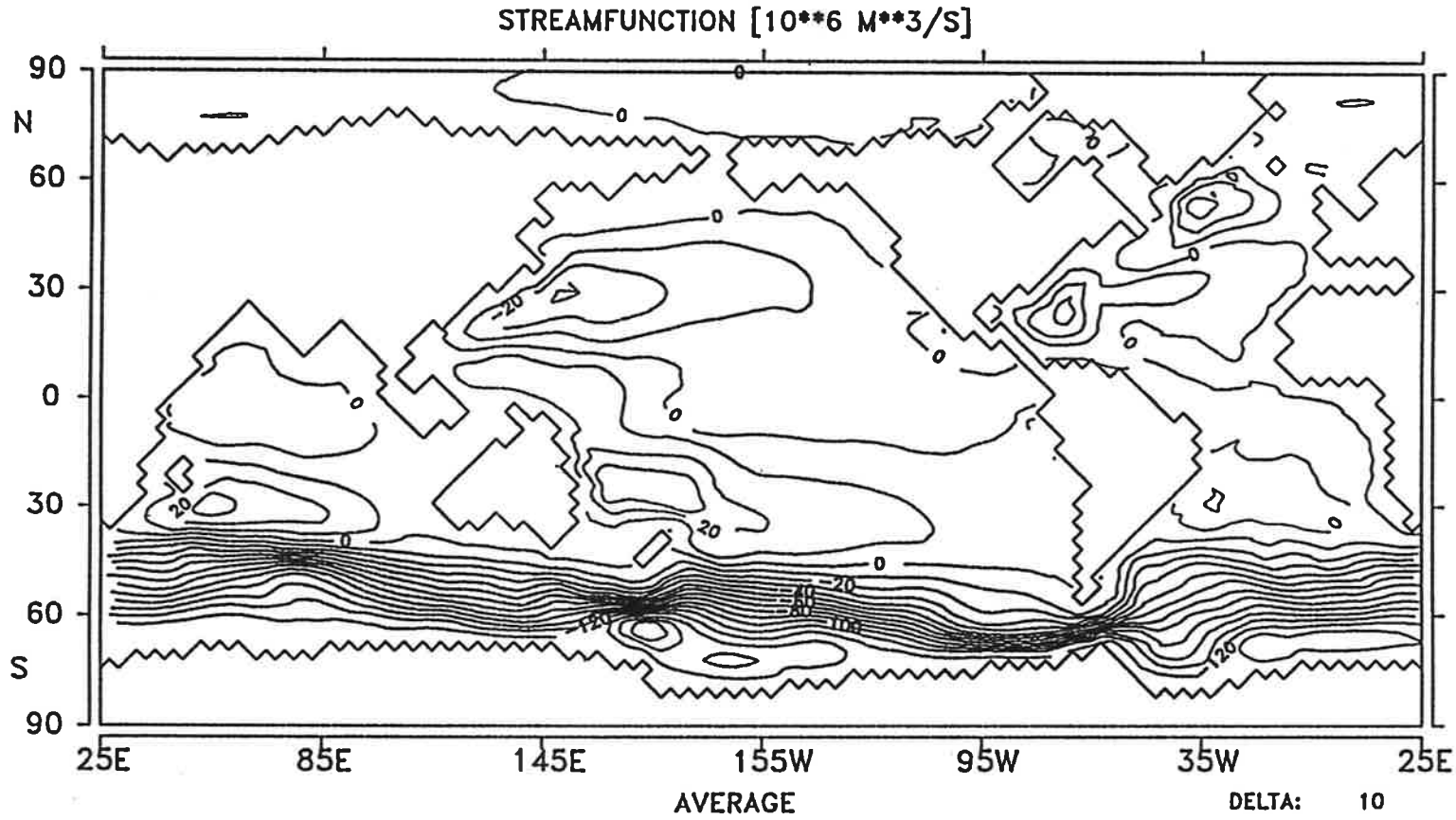

Fig. 4b Mass transport stream function

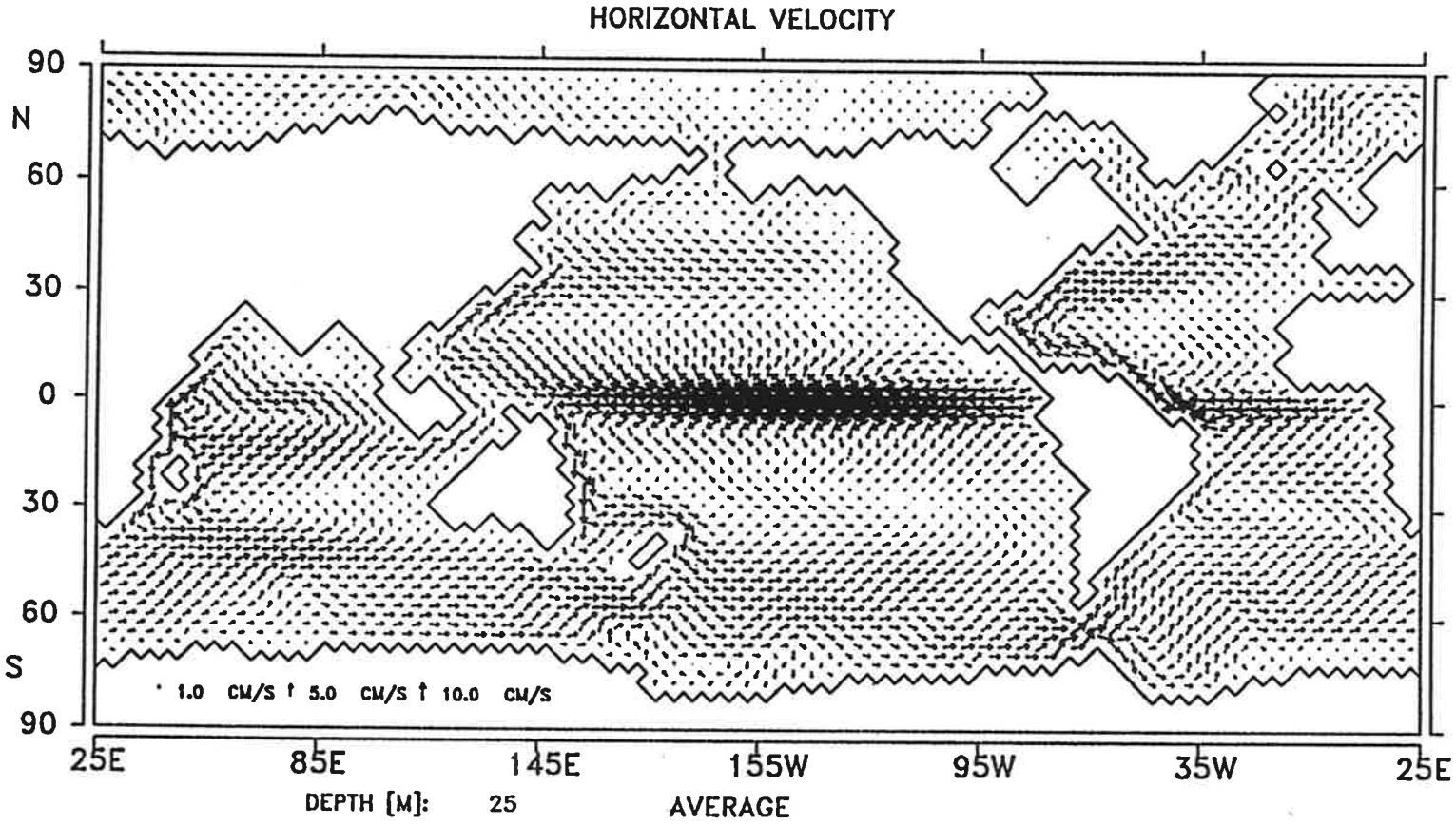

Fig.5a Horizontal velocity in the surface layer

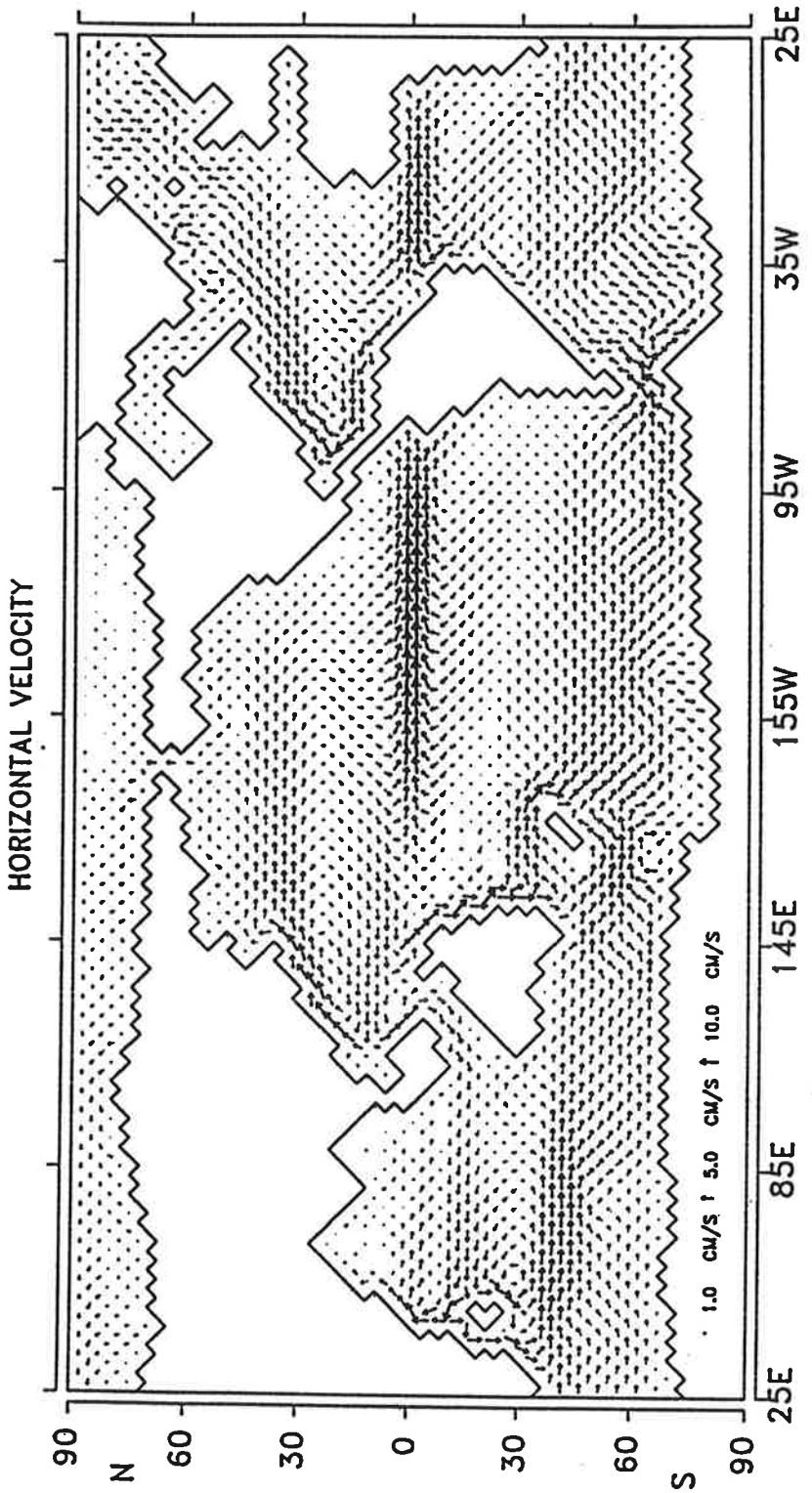

Fig.5b Horizontal velocity in the second layer

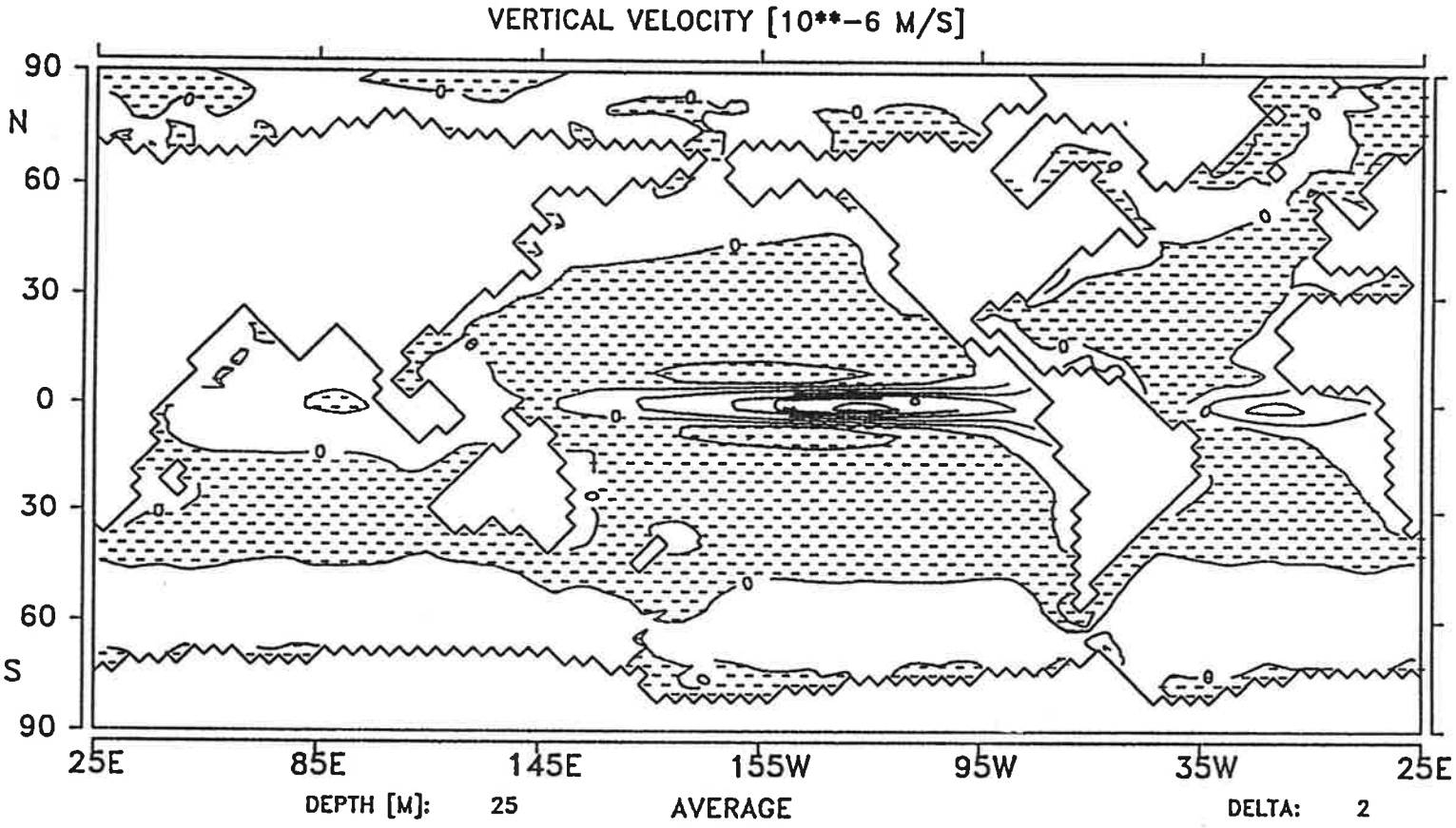

Fig.5c Vertical velocity below the first layer

slightly smaller, despite the much smaller geographical area of the North Atlantic compared with the full zonal extent of the Southern Ocean.

Figs. 3b and 3c show the individual meridional circulation patterns for the Atlantic and Pacific, respectively. The difference between the two oceans is pronounced. The tropical Pacific exhibits a rather symmetrical Ekman circulation in the upper kilometer and a deep inflow from the Antarctic sea, which ventilates the North Pacific. In the Atlantic, the surface Ekman cells are much weaker and the deep Atlantic is characterized by a strong outflow from the Arctic sea and a small bottom inflow from the south.

It should be kept in mind that the transports shown in Fig. 3 do not represent the total water exchange. A significant fraction of the total exchange occurs through convective mixing due to unstable stratification and also through vertical motions in limited regions, which are averaged out in the zonal integrations shown in Fig. 3a - c. This is particularly relevant in applications to tracer studies.

Fig.4 shows the surface topography and the vertically integrated mass transport stream function. The most pronounced feature is the strong Antarctic Circumpolar Current, which is associated with a large change of the surface elevation. The structure of the subtropical gyres is reproduced reasonably well. The Gulf stream, however, is underestimated by a factor of order two (which is typical for coarse resolution non-eddy resolving models).

The basic structure of the near surface circulation is shown in Fig.5. In the surface layer, the horizontal velocities (Fig.5a) consist of a superposition of the Ekman drift and the geostrophic current. The principal ocean surface current systems are reproduced quite well. The currents in the second layer (Fig.5b) closely follow the surface currents, except along the equator, where - despite the limited resolution and missing nonlinear advection of momentum - a realistic eastward undercurrent is simulated. The vertical velocity at the 50 m level is shown in Fig.5c. It is determined by the divergence of the net surface current, which at this level is dominated by the Ekman transport.

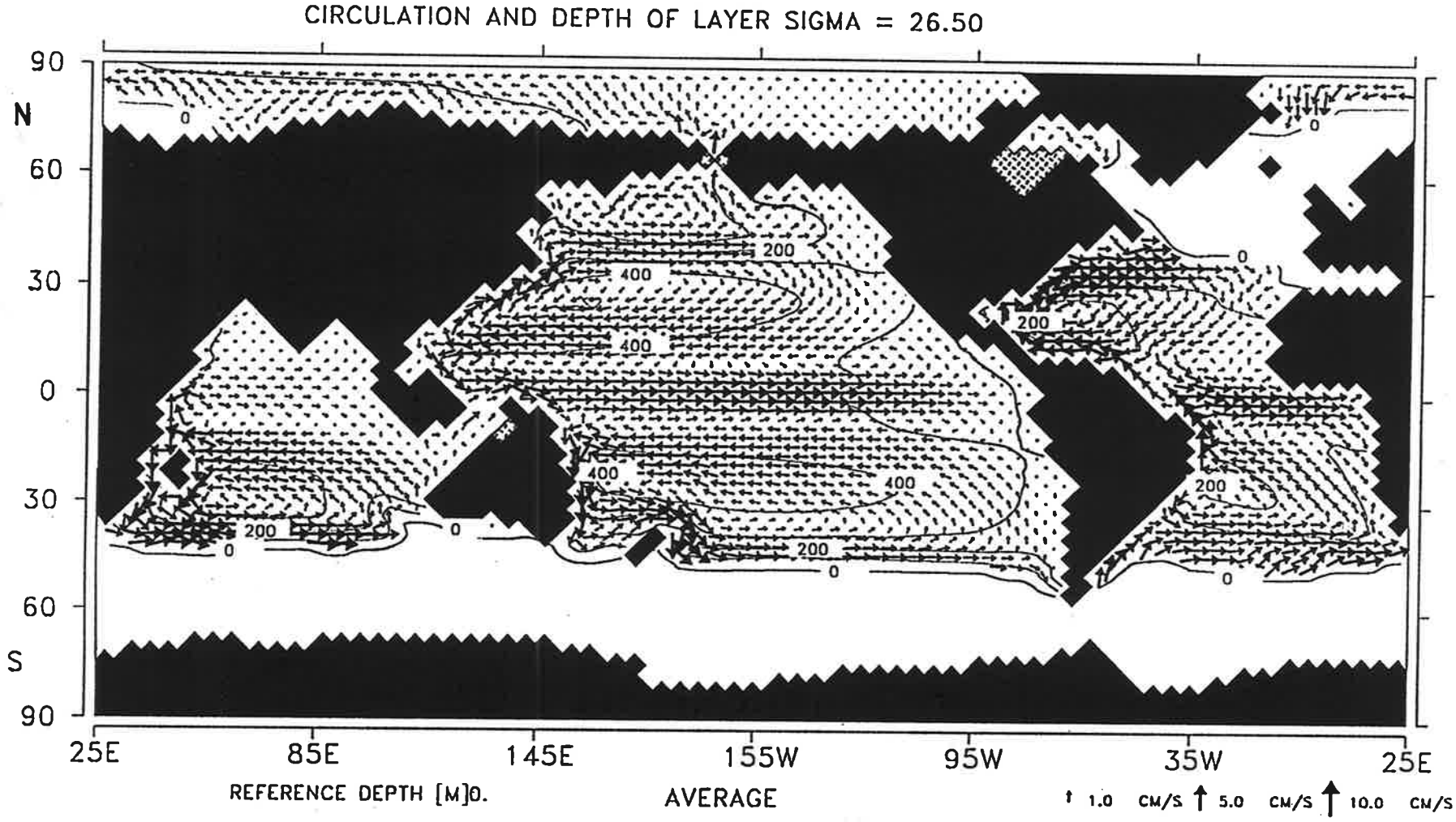

Fig.6a Depth of the layer σ_ϑ = 26.5 and circulation in this horizon

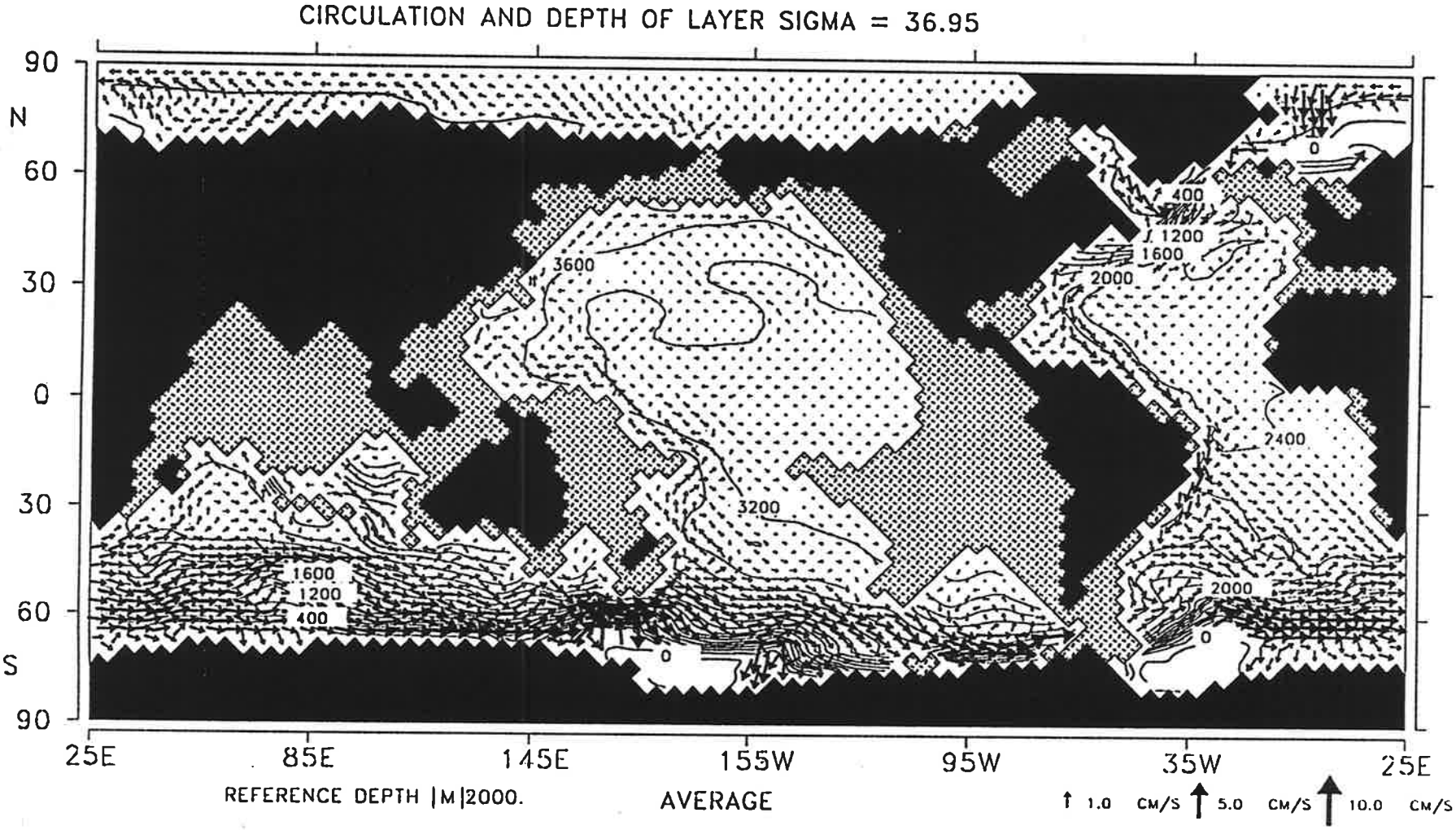

Fig. 6b Depth of the layer σ_2 = 36.95 and circulation in this horizon

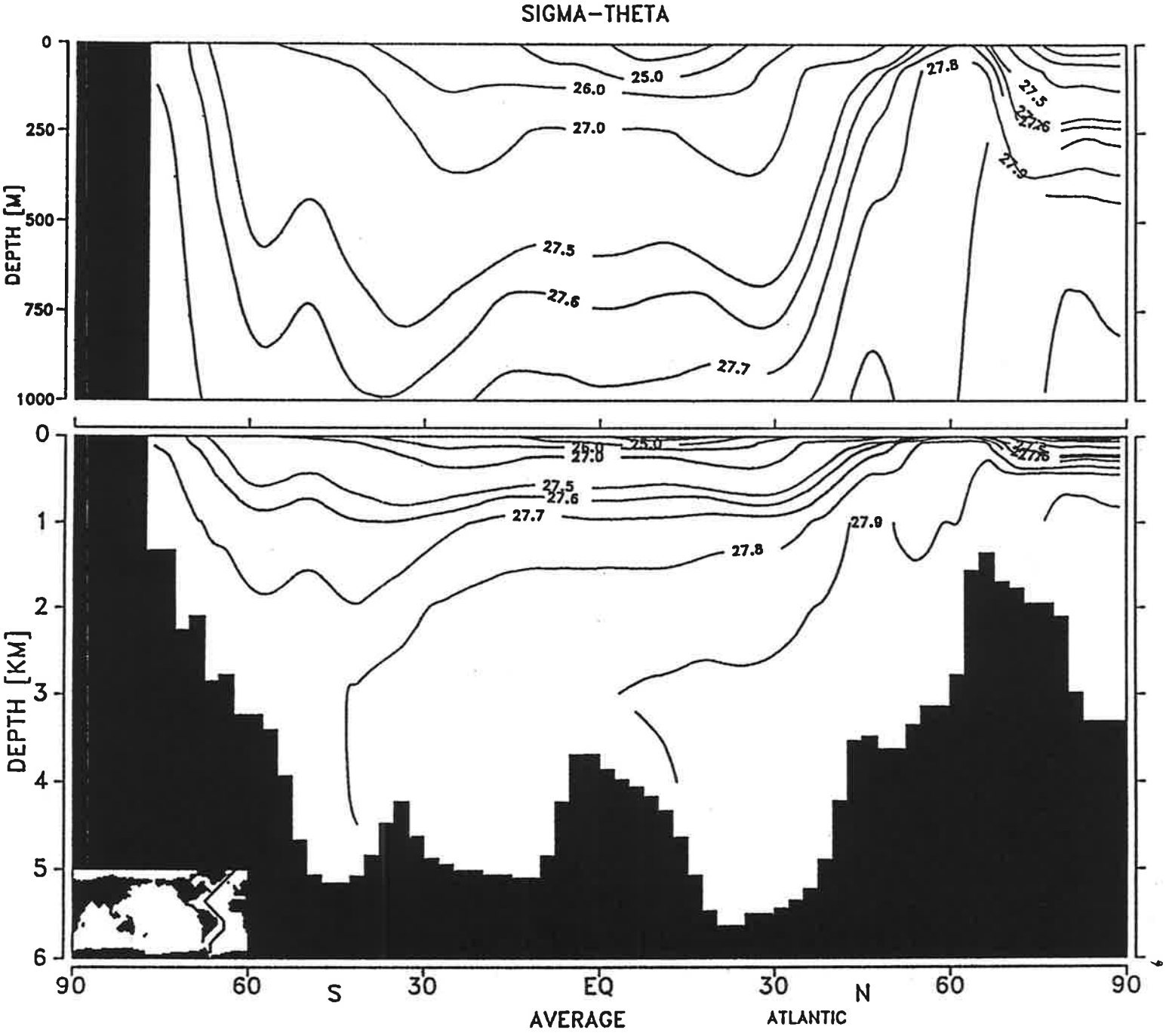

Fig.7a σ_ϑ in a section of the western Atlantic

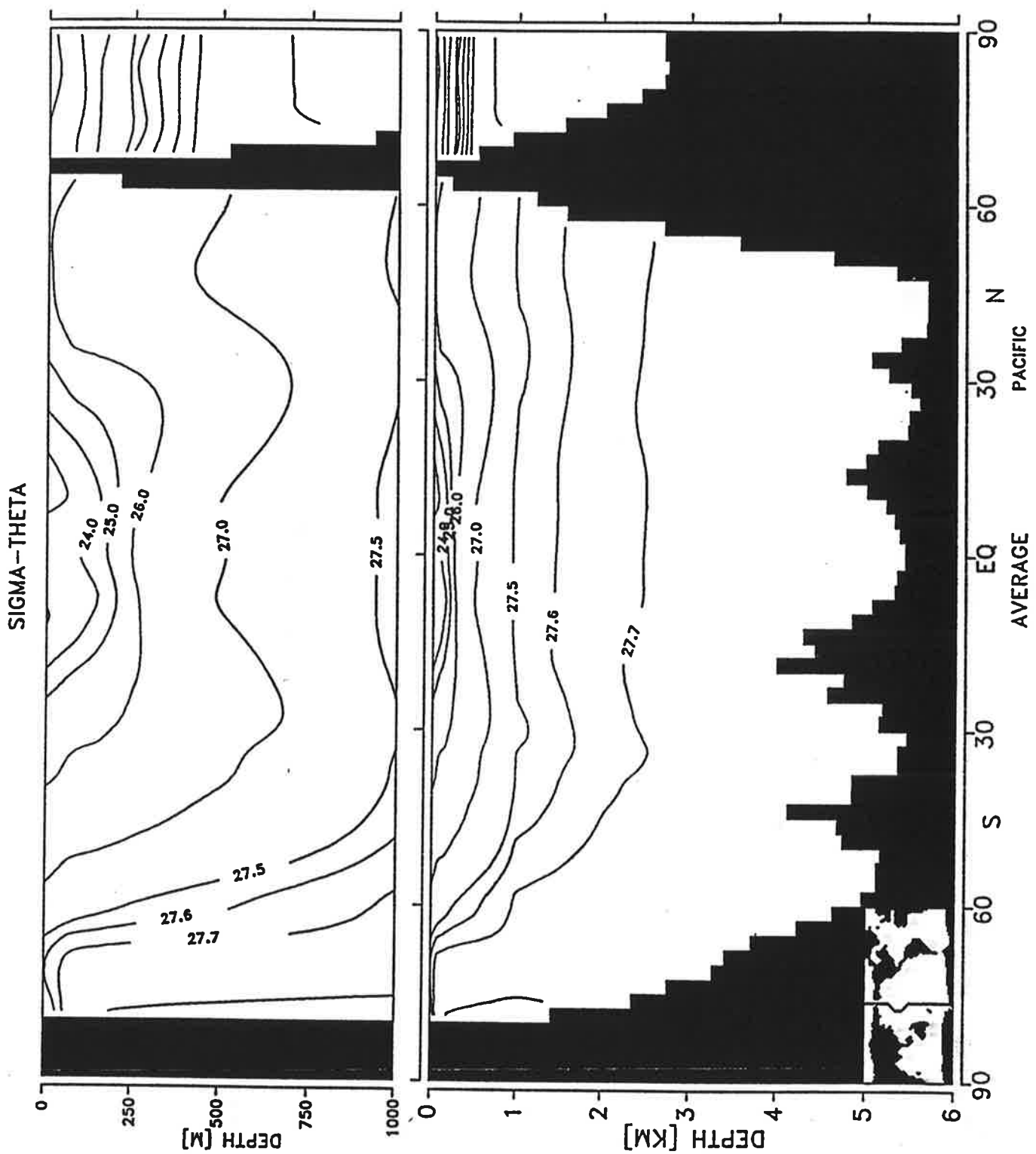

Fig.7b σ_ϑ in a section of the western Pacific

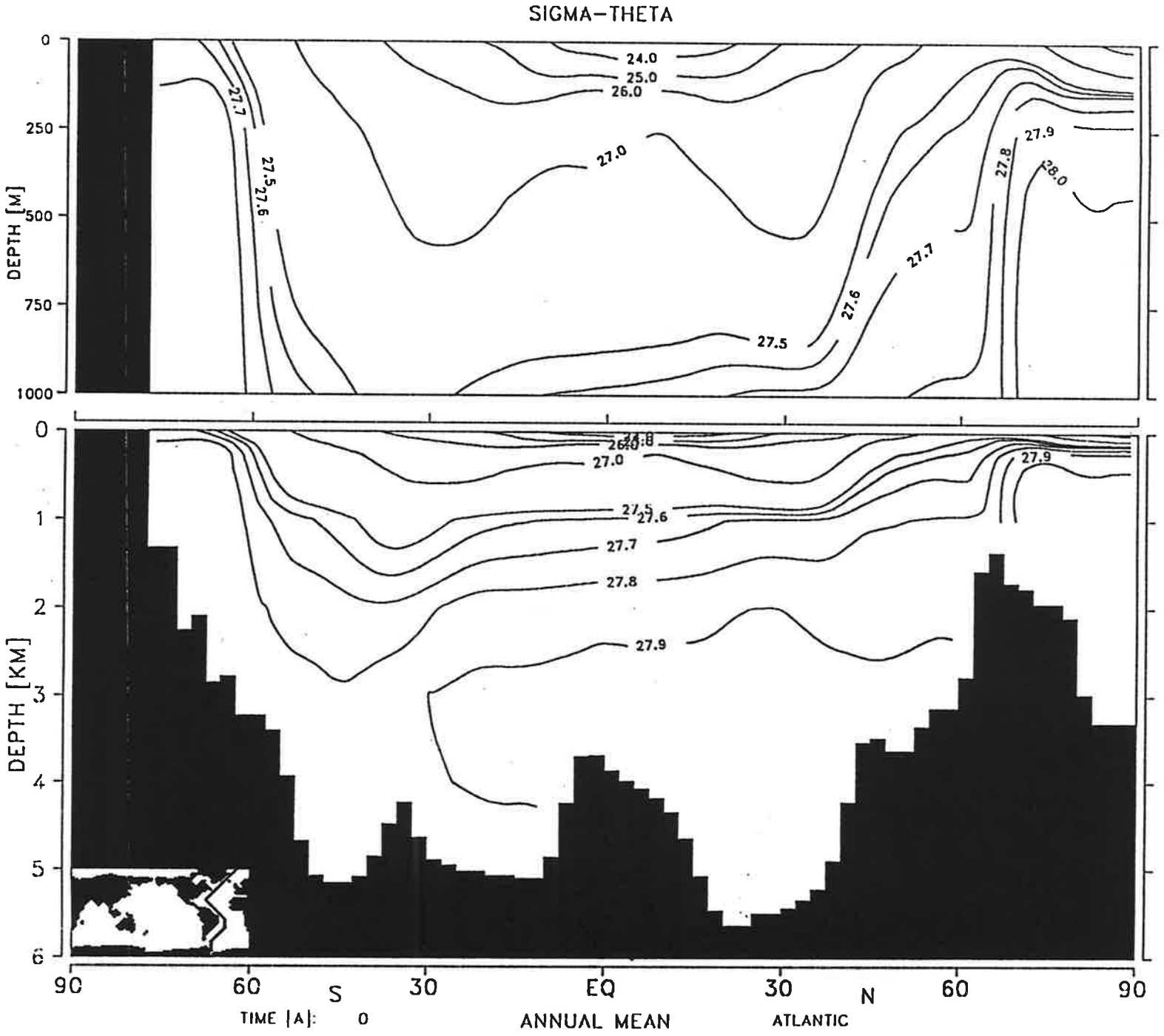

Fig.7c Same as 7a from the Levitus data set

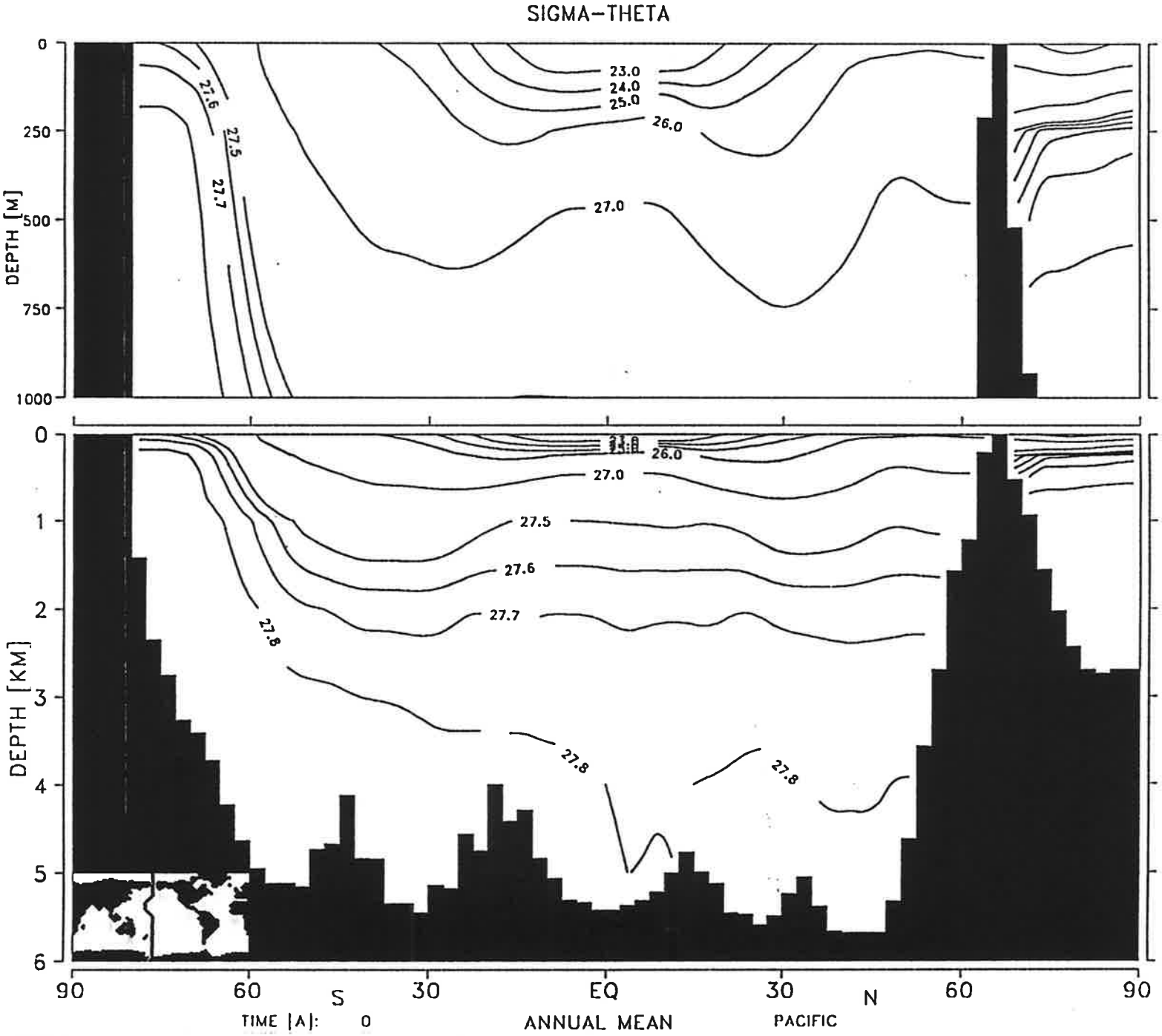

Fig. 7d Same as 7b from the Levitus data set

The structure of the water mass transport in deeper levels is best represented by the flow field along surfaces of constant density. As potential density is approximately conserved below the mixed layer, all water parcel trajectories should follow these surfaces rather closely. Figs. 6a,b show the depths of the isopycnal surfaces σ_ϑ=26.5 and σ_2=36.96, respectively, together with the associated horizontal velocity fields. The surface σ_ϑ = 26.5 characterizes the main thermocline gyres and the equatorial undercurrent, while the isopycnal σ_2= 36.96 lies in the deeper ocean. For this level, the 2 km reference depth potential density σ_2 was chosen rather than the surface reference level, since σ_ϑ is no longer appropriate because of the nonlinearity of the equation of state (cf., for example, the GEOSECS (Bainbridge, 1981) section for σ_ϑ in the Atlantic, which displays a spurious apparent instability in the deep southern region through this effect). The equatorial upwelling region and the depression of the isopycnals in the main gyres are clearly seen. In most regions of the ocean, the flow follows the constant depth contours, but isobaths are crossed in areas of upwelling and downwelling. Near the outcropping boundaries, however, variations in the isopycnal depth are generally the result of water mixing rather than adiabatic rising or sinking motions.

Figs.7 a,b show two sections of σ_ϑ in the Pacific and Atlantic computed from S and T. The most outstanding feature is the doming of the isopycnals across the equator (the apparently unstable stratification in the deep Atlantic is again spurious and arises from the difference in the gradients of σ_4 and σ_ϑ). The observed data show additionally a pronounced tongue of antarctic intermediate water, especially in the South Atlantic salinity. This structure appears also in the model, but is underestimated.

These sections can be compared directly with the corresponding sections of the Levitus data set displayed in Figs 7 c,d. The model results agree quite well with the climatological data set. The agreement in temperature and salinity separately, however, is less marked; the errors seem to cancel each other with respect to their influence on the density. Figs. 7 e,f show the Atlantic sections of salinity from the Levitus data and from the model. The general structure is well

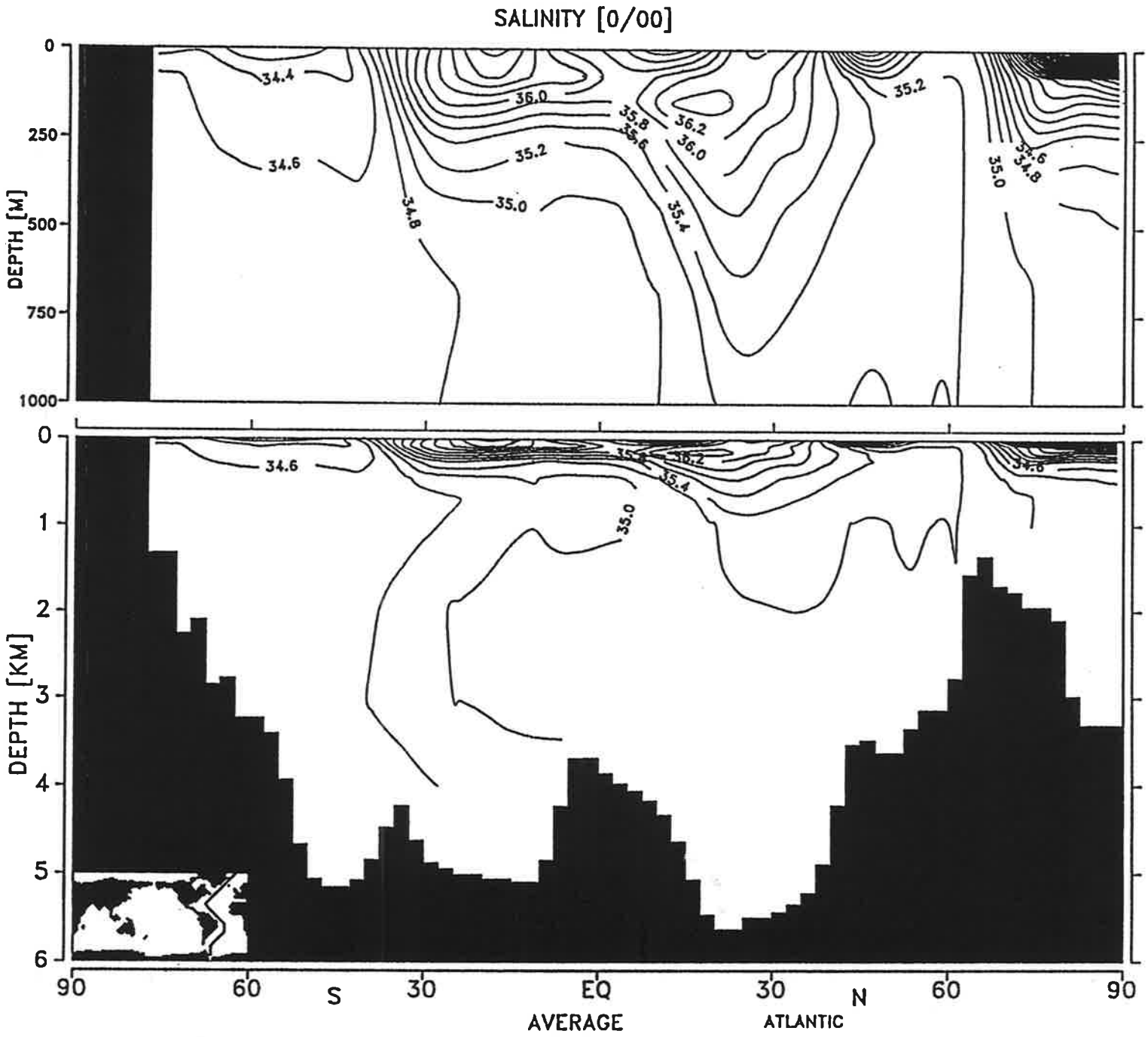

Fig.7e Salinity section in the western Atlantic

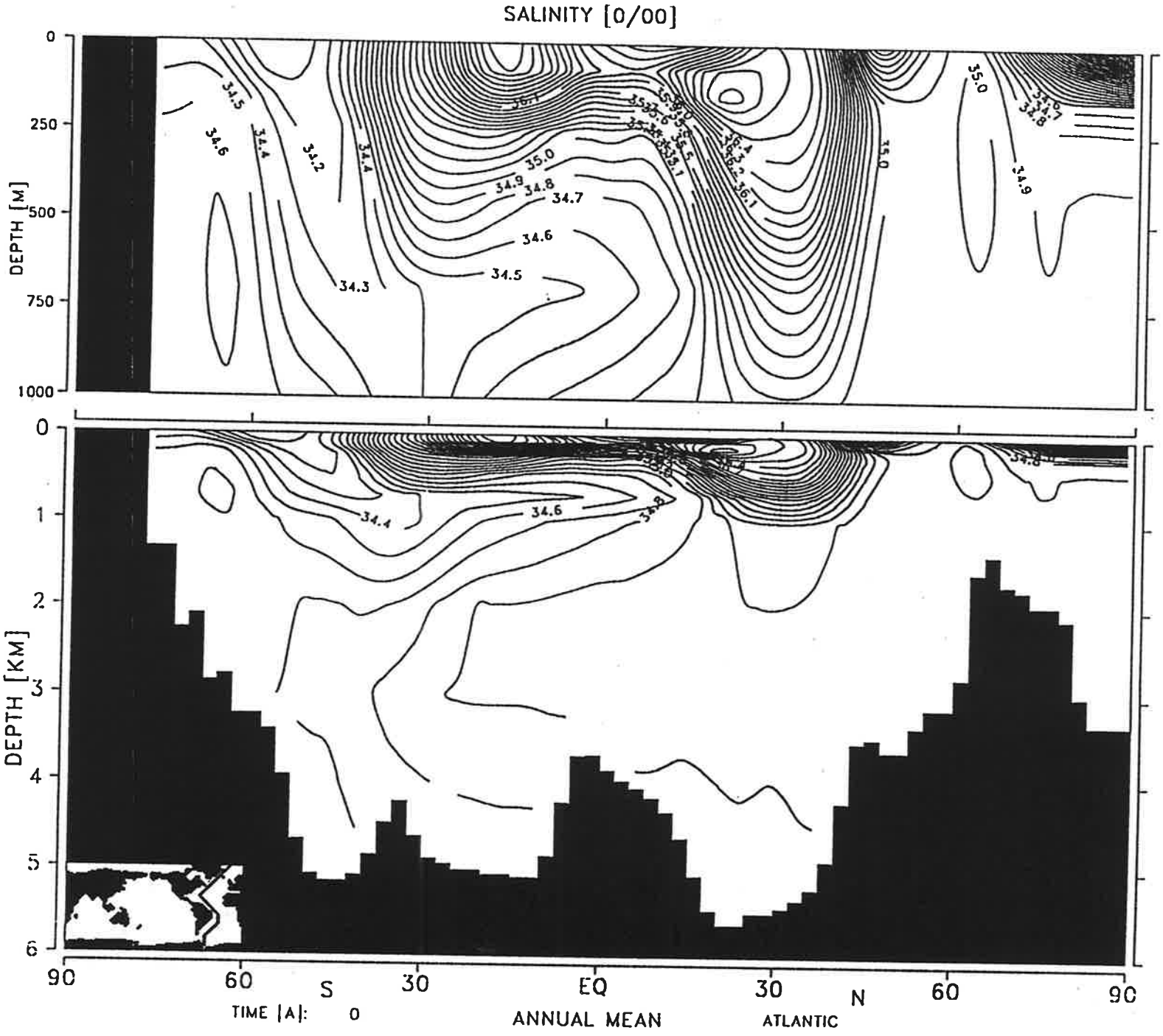

Fig.7f Same as 7e from the Levitus data set

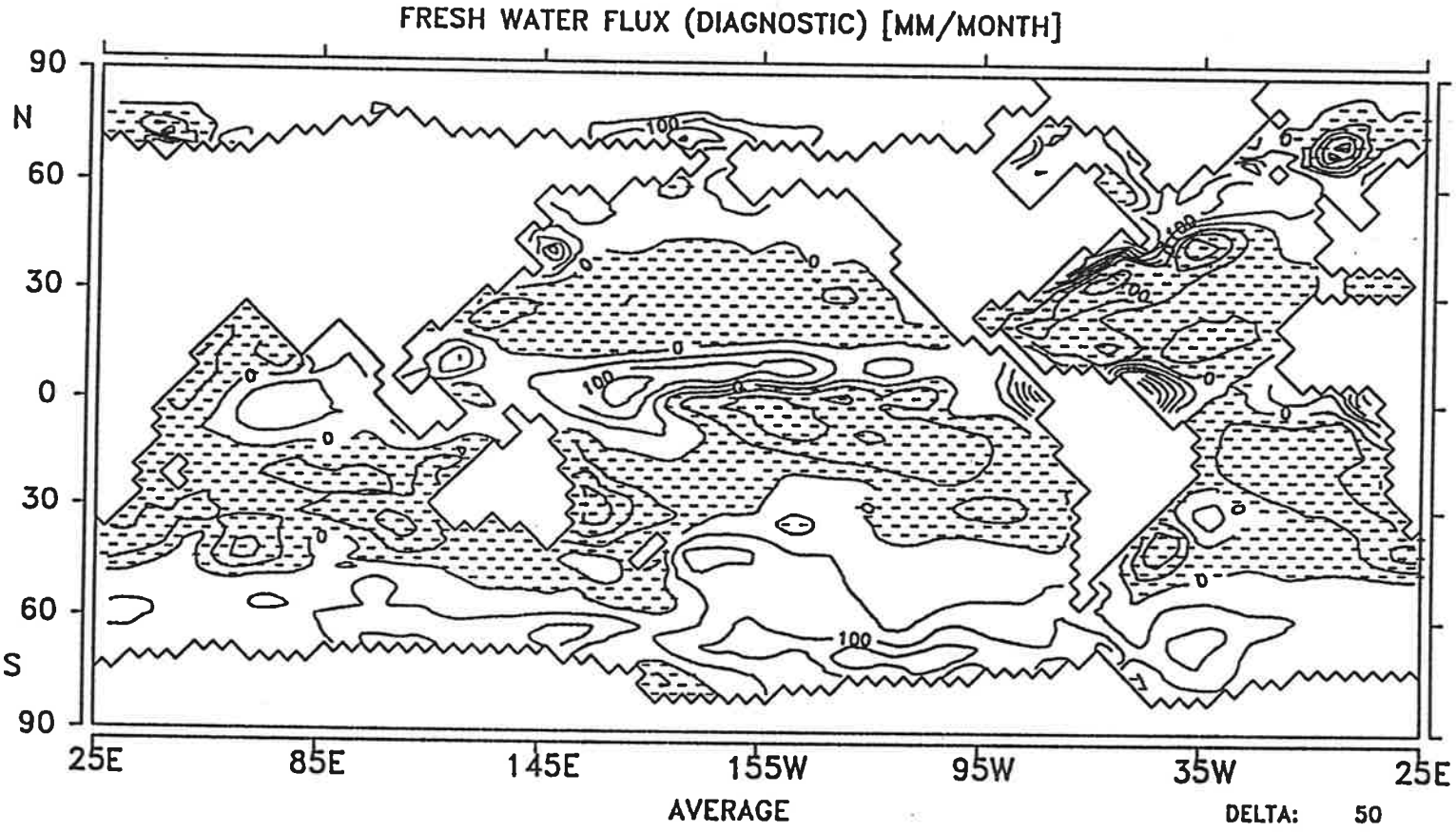

Fig. 8 Freshwater flux as determined diagnostically from the salinity boundary condition.

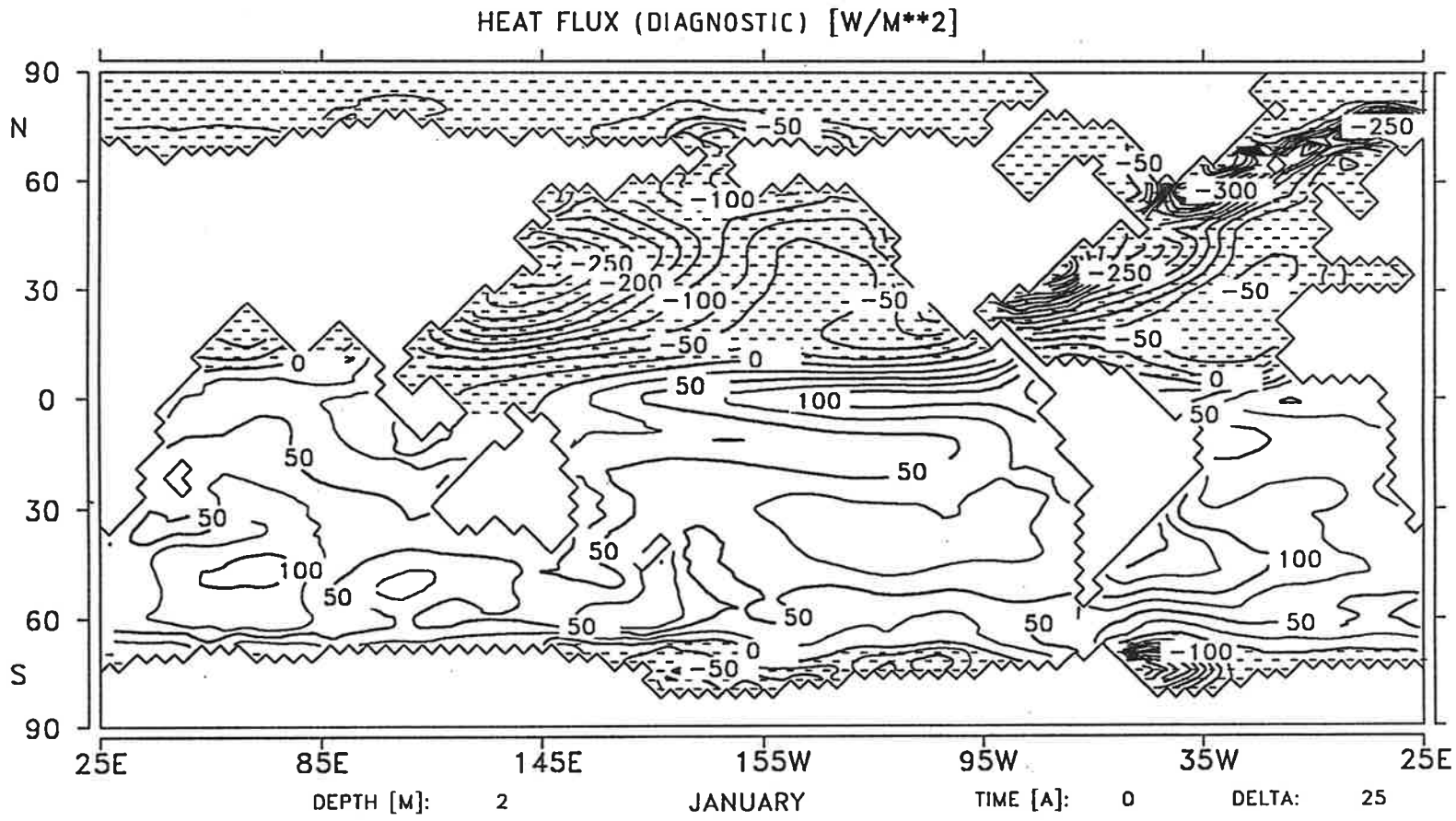

Fig. 9a Heat flux as determined diagnostically from the temperature boundary condition for January

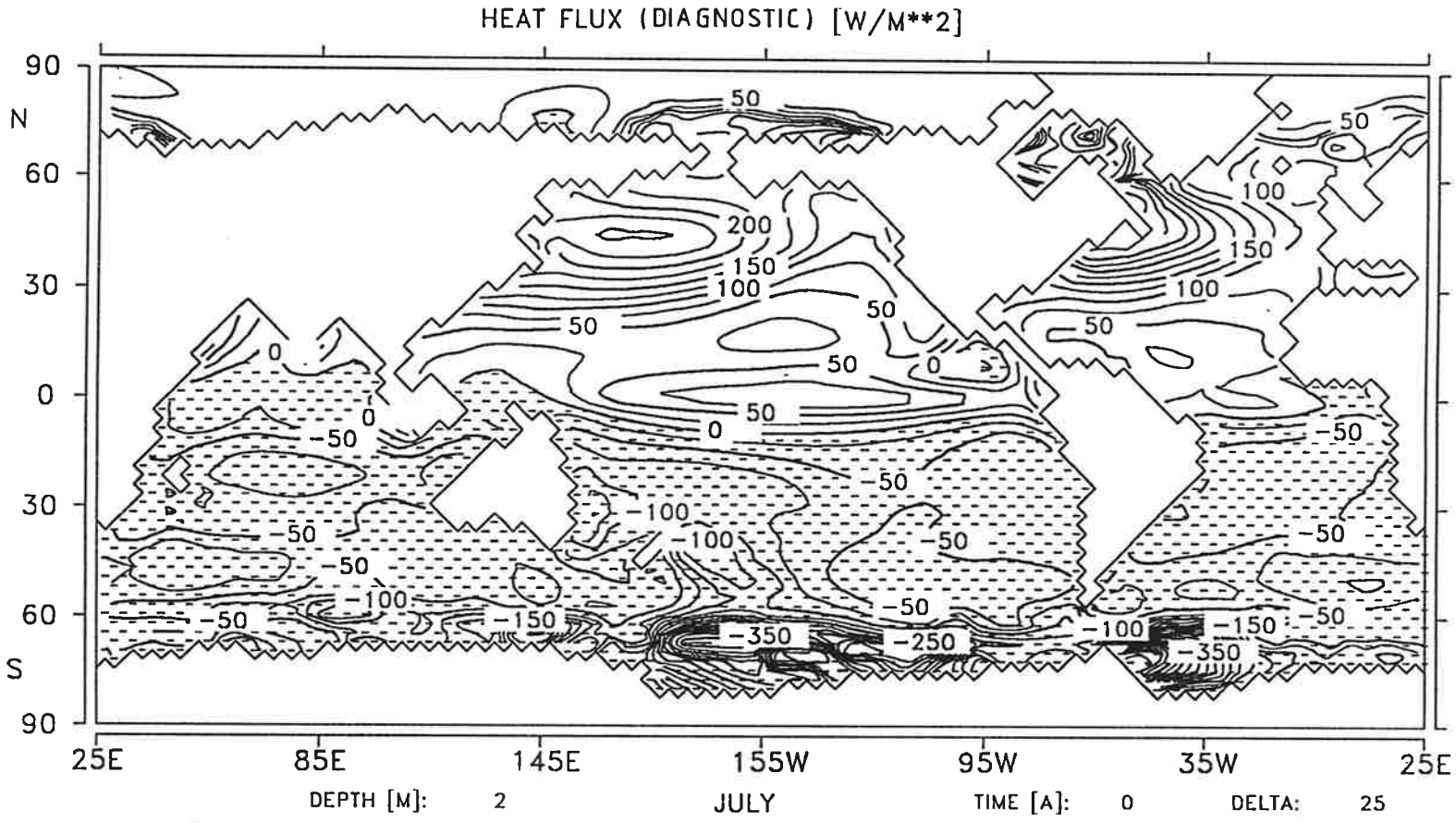

Fig. 9b Heat flux as determined diagnostically from the temperature boundary condition for July

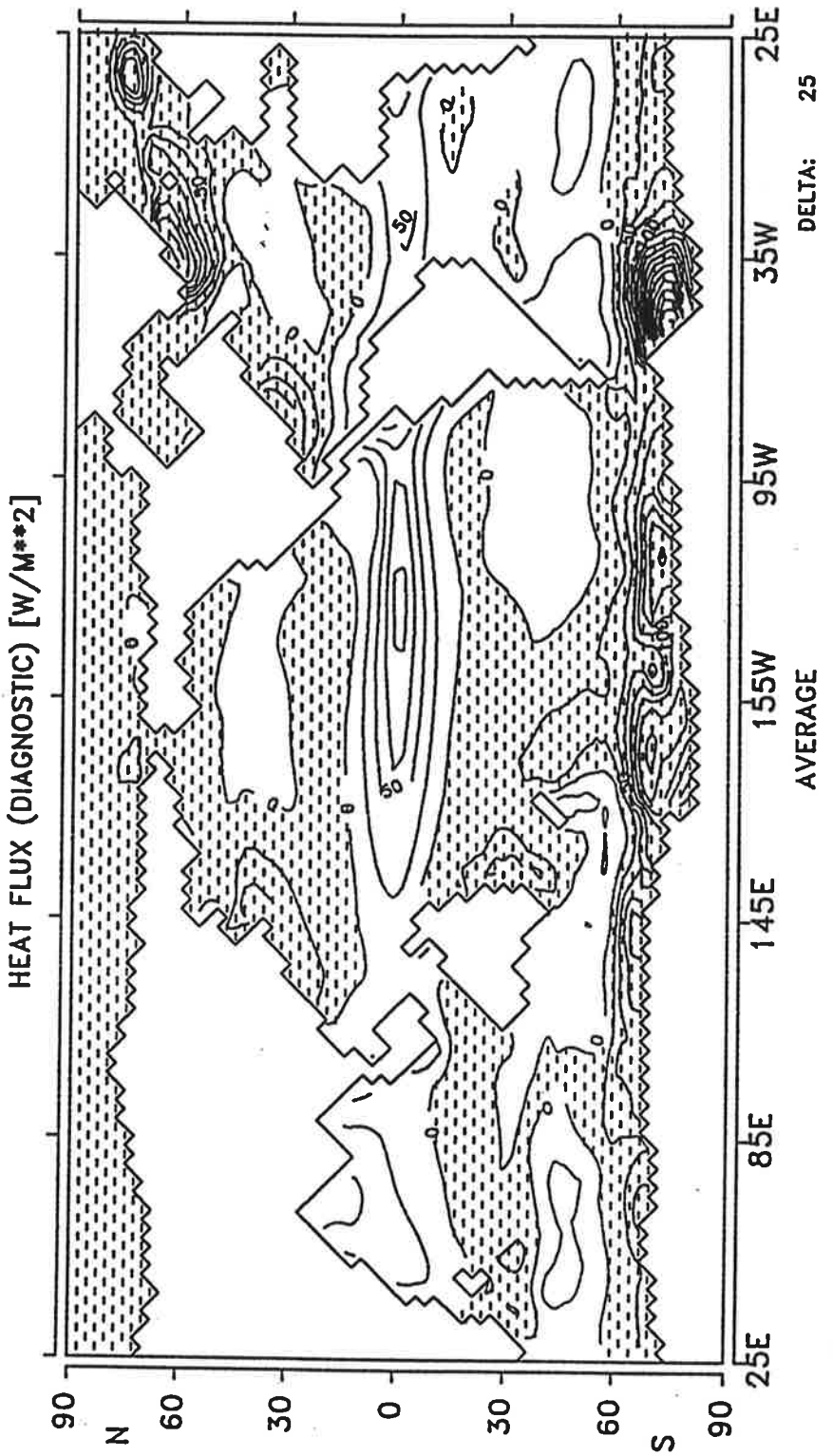

Fig. 10 Same as Fig. 9, annual mean

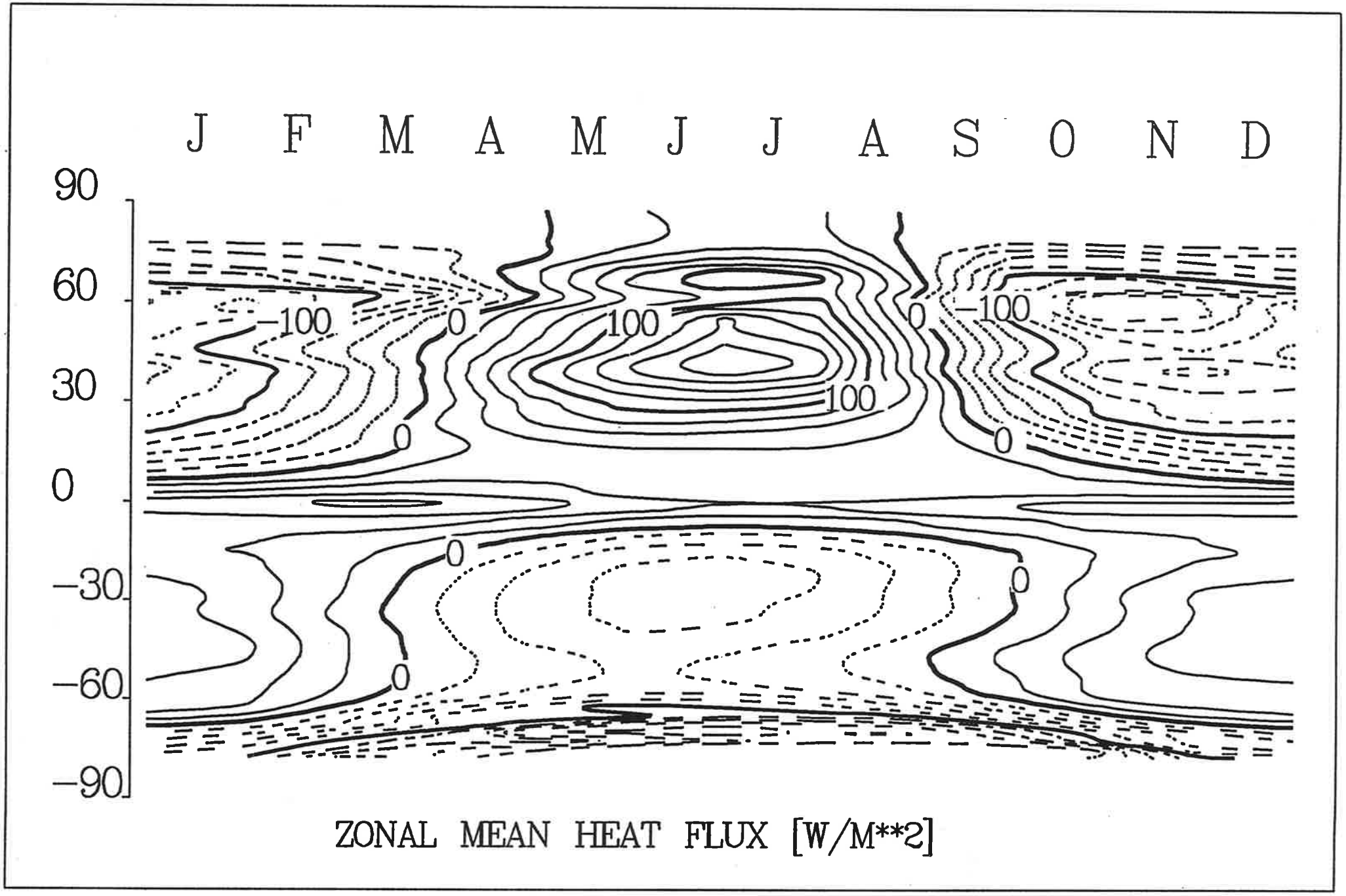

Fig. 11 Seasonal cycle of the zonally integrated heat flux

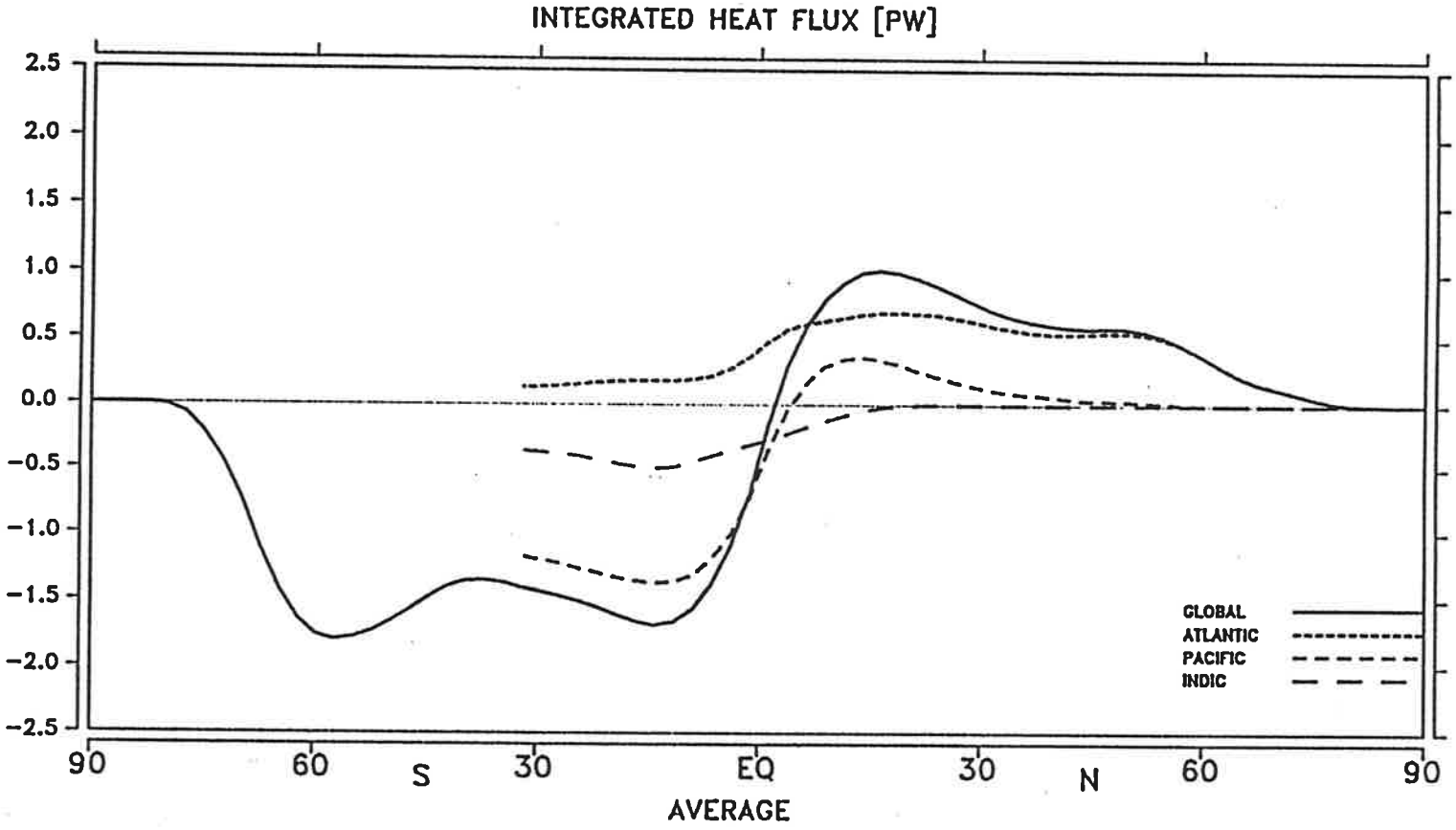

Fig. 12a Zonally integrated transport of heat(annual mean)

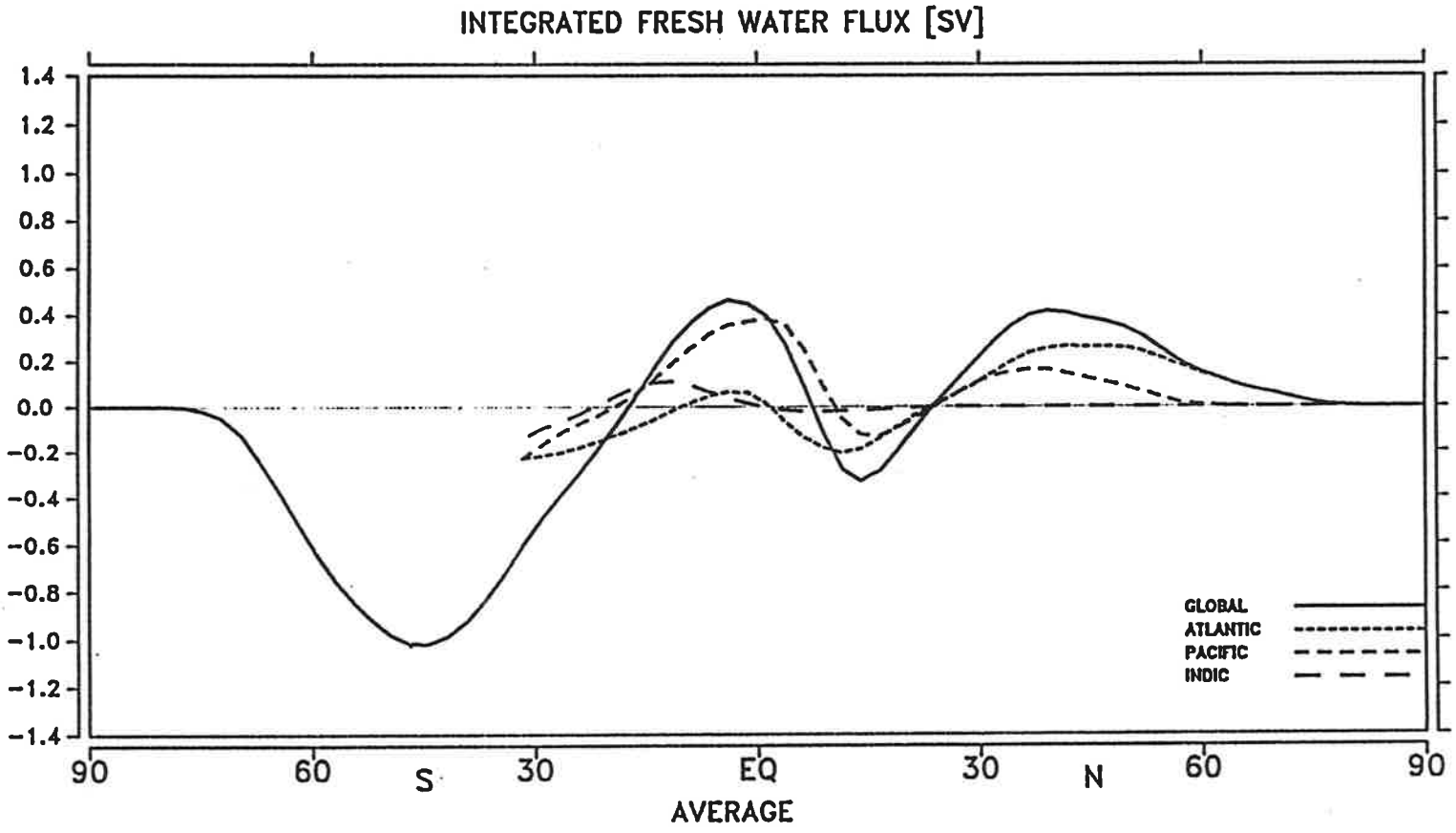

Fig. 12b Integrated fresh water flux

reproduced; the models salinity, however, is slightly too high, as seen most clearly in the tongue of Antarctic intermediate water.

The surface fluxes of fresh water and heat, computed diagnostically from the boundary values of salinity and temperature, are shown in Figs. 8 and 9, respectively. Characteristic regional features, such as theevaporation in subtropical gyres and increased precipitation in the North Pacific, are reproduced as expected. In the polar regions, the fresh water flux is influenced by changes in the ice budget in addition to the evaporation - minus - precipitation budget.

The seasonal heat flux distributions (Fig. 9, for January and July) exhibit strong regional variations (for example in the South Pacific), which are not easily interpreted. However, these variations largely cancel out in the annual mean heat flux (Fig. 10), which resembles rather closely the pattern derived from observations (e.g. Esbenson and Kushnir, 1981, or Oberhuber, 1988). The seasonal cycle of the zonally integrated heat flux (Fig.11) also agrees quite well with observed data.

Fig 12, finally, shows the zonally integrated meridional transports of heat and salt in the three seperate ocean basins. The striking differences between the circulation patterns in the different ocean basins, discussed already in terms of the "conveyor belt" picture, appear also in the meridional transports. The Atlantic exhibits a substantial northward heat transport in both hemispheres, extending across the equator up to Iceland, whereas the heat transport of the Pacific is very small outside the equatorial Ekman circulation region.

4. Sensitivity with respect to temperature and salinity surface boundary conditions

We investigate now the dependence of the ocean circulation on alternative formulations of the boundary conditions for heat and salt. In addition to the standard run ATOS1 (Atmospheric Temperature, Ocean Salt and atmospheric temperature advection with reference factor 1), four further experiments were carried out (cf.Table 1). These differed in the temperature boundary condition (coupling to the observed ocean surface temperature in OTOSE, OTOSD or to the observed atmospheric surface temperature with different advection factors in ATOS0/1/2) and in the

relaxation time constants used for the temperature and salinity boundary conditions. All cases could be regarded as acceptable interpretations of climatology and could therefore be expected intuitively to give similar results. However, the simulations were in fact found to differ significantly.

Table 1

name	OTOSD	OTOSE	ATOS0	ATOS1	ATOS2
salinity restoring time constant	1500 d	30 d	40 d	40 d	40 d
temperature restoring time constant	30 d	30 d	60 d	60 d	60 d
forcing temperature	SST	SST	air	air	air
sea ice model	no	no	yes	yes	yes
air temperature restoring time constant λ^{-1}	--	--	0	$1.2\ 10^5$s	$2.4\ 10^5$s

The most pronounced differences between the five experiments appeared in the circulation regime of the deep ocean. This strongly affects the residence times of tracers, the rate of uptake of CO_2 by the oceans and the heat and fresh water transports (which are intimately linked with the meridional overturning). The deep ocean temperatures and salinities also differ to some extent (Fig. 13). However, it is difficult to judge the model performance from these fields alone, as the observed deep ocean values could well represent the response to ocean surface conditions several hundred years ago (during the little ice age).

The ocean currents and density stratification in the upper ocean are only weakly influenced by the modifications in the boundary conditions.

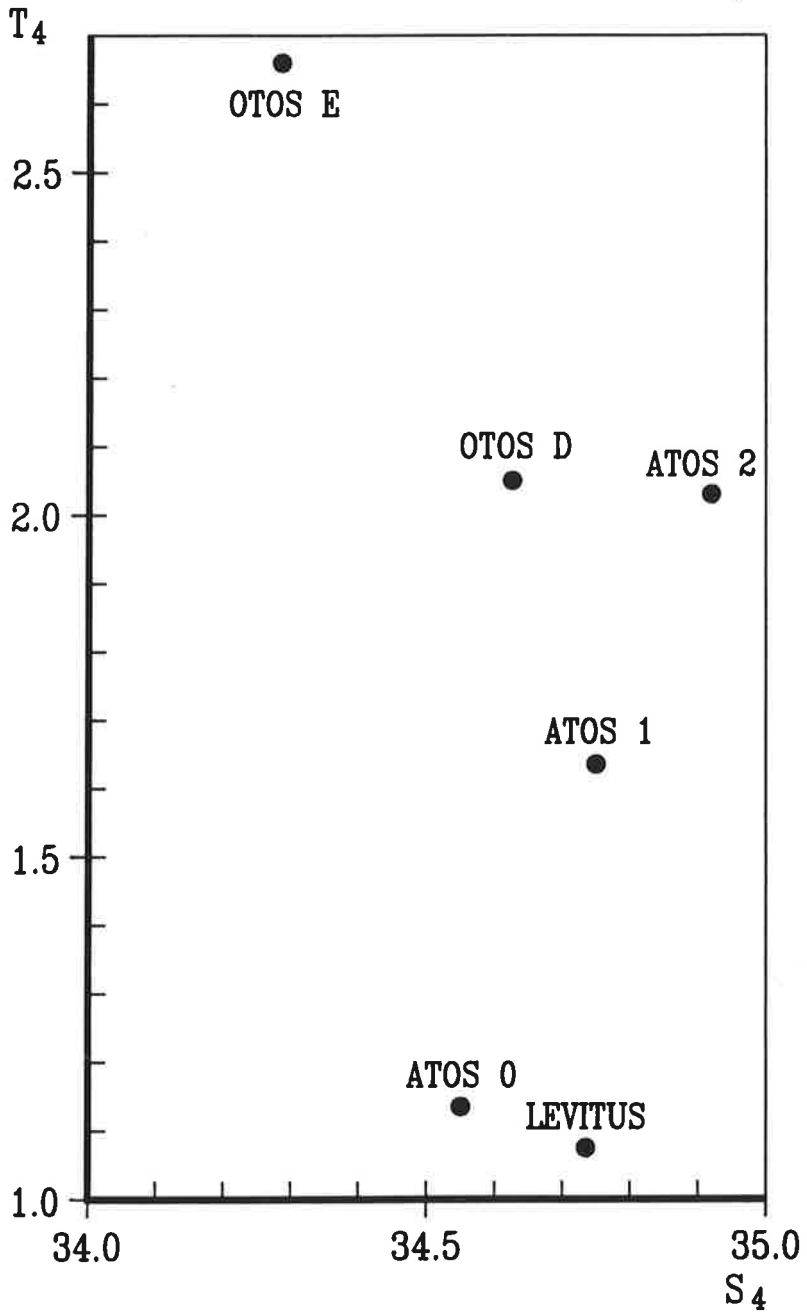

Fig. 13 Global averages of temperature and salinity at a depth of 4 km for the five experiments and from Levitus

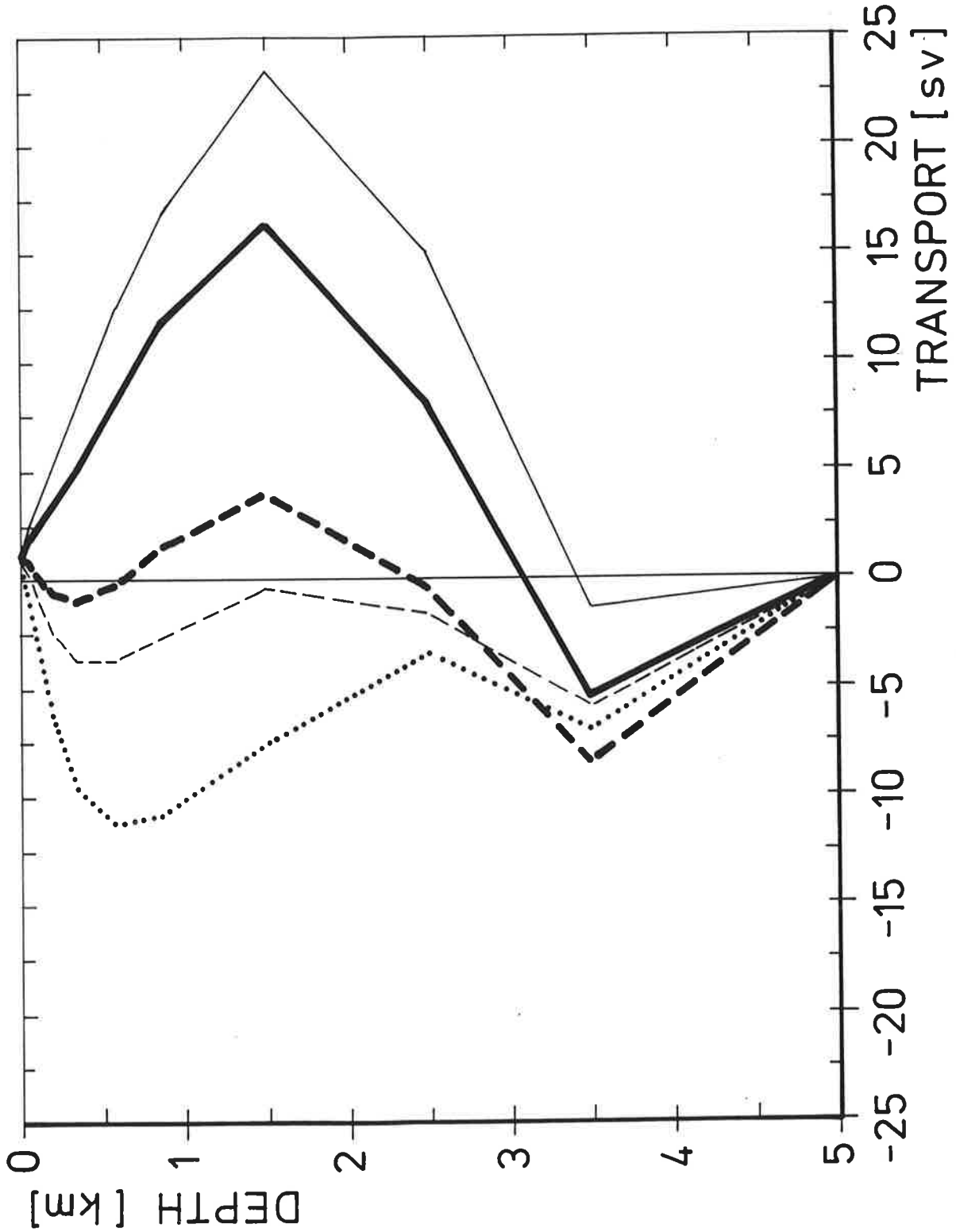

Fig.14 Zonally integrated flow across 30^{0} S in the Atlantic for the five experiments

It appears that the main wind driven gyres are not very sensitive to the form of the heat and fresh water flux boundary condition (the wind stress was not changed in the sensivity experiments shown, but in other simulations with modified wind fields significant changes in the ocean gyres were not found).

Fig. 14 shows a comparison of the meridional overturning stream functions of the Atlantic circulation for the five experiments. While the standard run ATOS1 produces a deep southward flow of 22 Sverdrup below a depth of 1,5 km in the North Atlantic - which is the source of the classical "conveyor belt" transport into the South Atlantic, the Indian ocean, and the Antarctic Circumpolar Current - the experiments OTOSE, OTOSD and ATOSø all fail to provide an adequate source of North Atlantic deep water. The cold deep water in the Atlantic flows northwards in these experiments from a source in the Southern Ocean. The experiment ATOS2 is similar to ATOS1, but exhibits, as expected, a too strong southward deep Atlantic flow.

In comparison with observed data, the differences in the flow regimes are best seen in the geochemical tracers. Fig. 15 compares the computed ^{14}C distribution for ATOS1 with the measurements of Östlund et al., 1976, Stuiver et al., 1980. An accurate computation of ^{14}C distributions requires a three dimensional carbon cycle model (cf. Maier-Reimer and Hasselmann, 1987; Bacastow and Maier-Reimer, 1990). However, for the present comparative purposes a simplified ^{14}C tracer model without a biological pump appeared adequate. The ^{14}C was assumed to enter the ocean from the atmosphere at an initial concentration of 1000 units with a constant piston velocity of 6m/year. It was then advected by the (previously computed) mean ocean circulation while decaying with an e-folding time of 8267 years. The vertical mixing by convection was estimated from the (also previously computed) frequency and intensity of convective mixing in the ocean circulation run.

In Fig 16 we compare the results of the five experiments with the GEOSECS data along the section in the western Atlantic in 3 km depth - which is approximately the core of the real NADW. For the assessment of the circulation fields, the gradients are more important than the

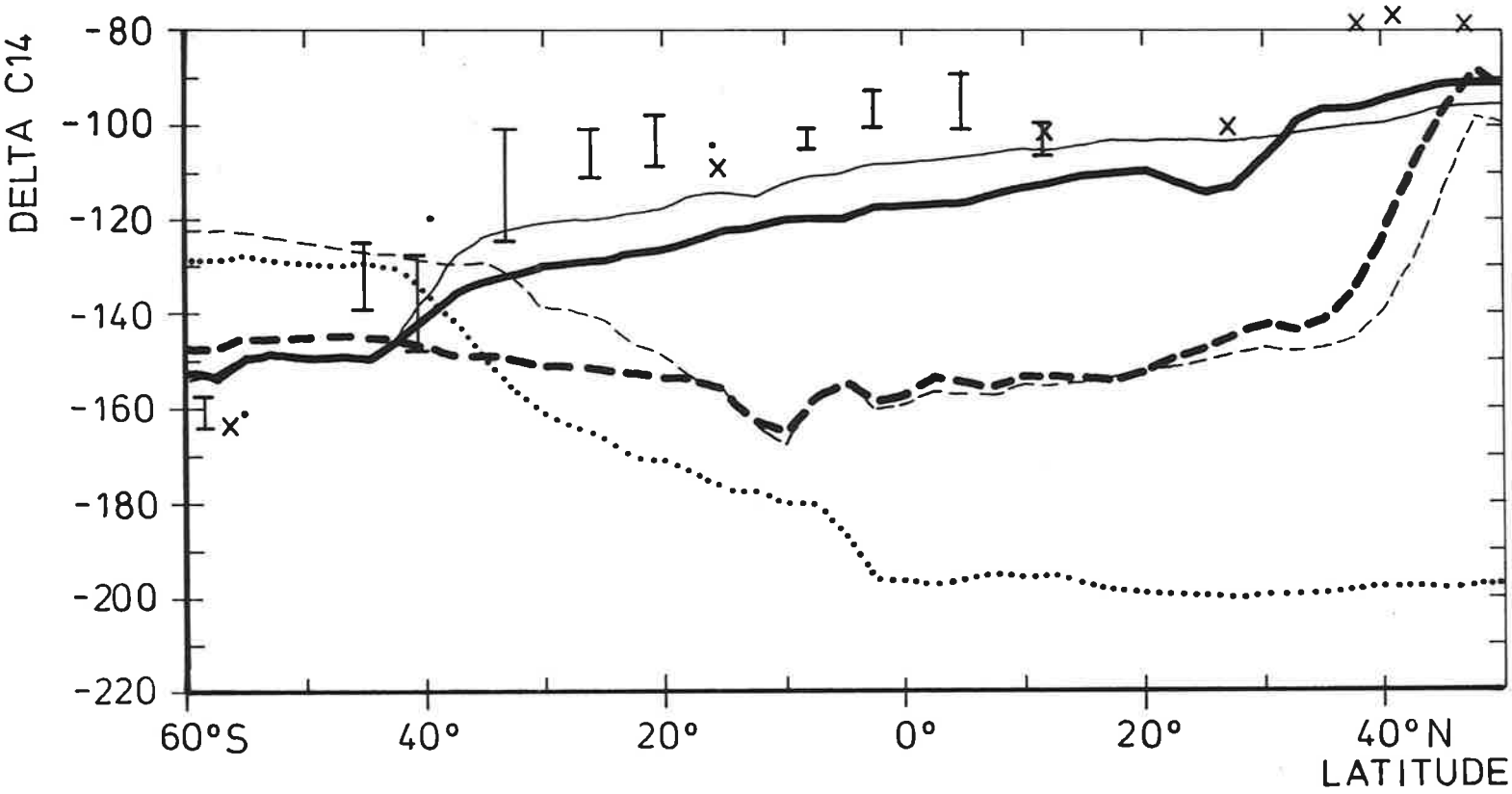

Fig. 15 Radiocarbon along a section in the western Atlantic for the five experiments and the GESOSECS data in 3 km depth

a)

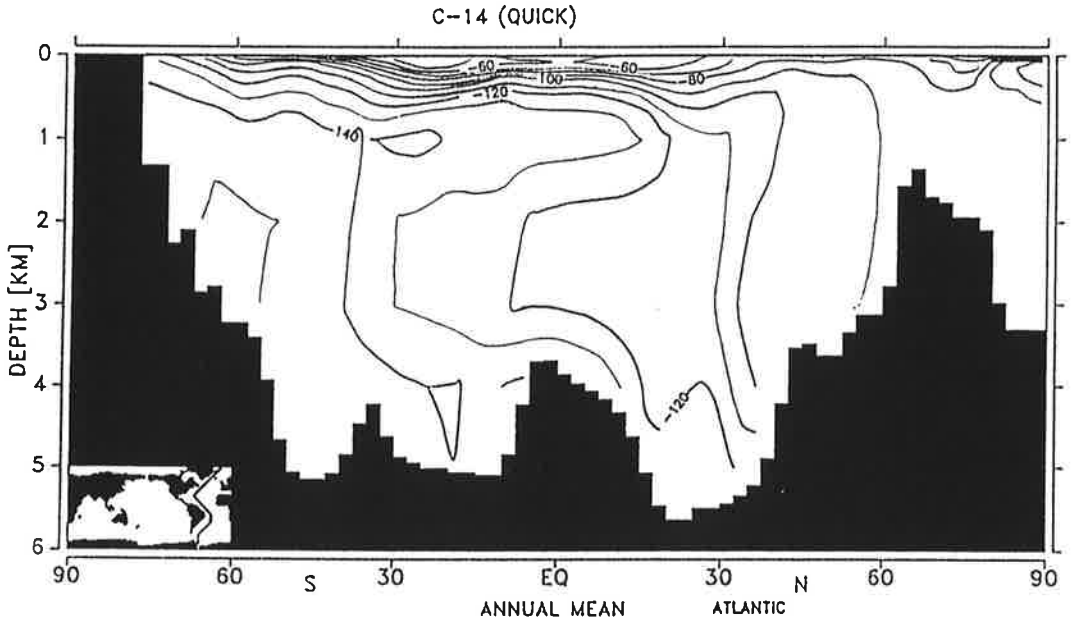

b)

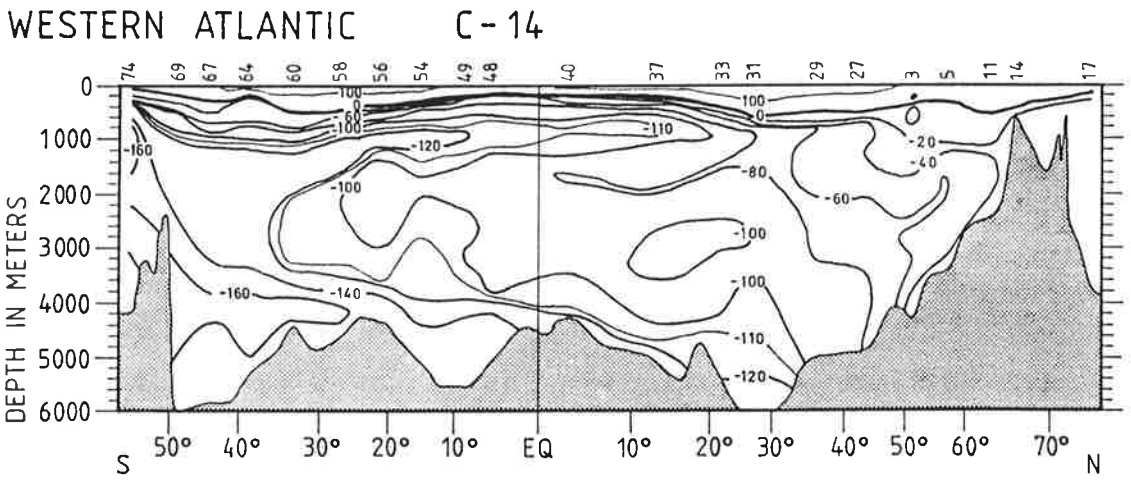

Fig. 16 Radiocarbon in the western Atlantic for the standard run (a) and from the GEOSECS atlas (b)

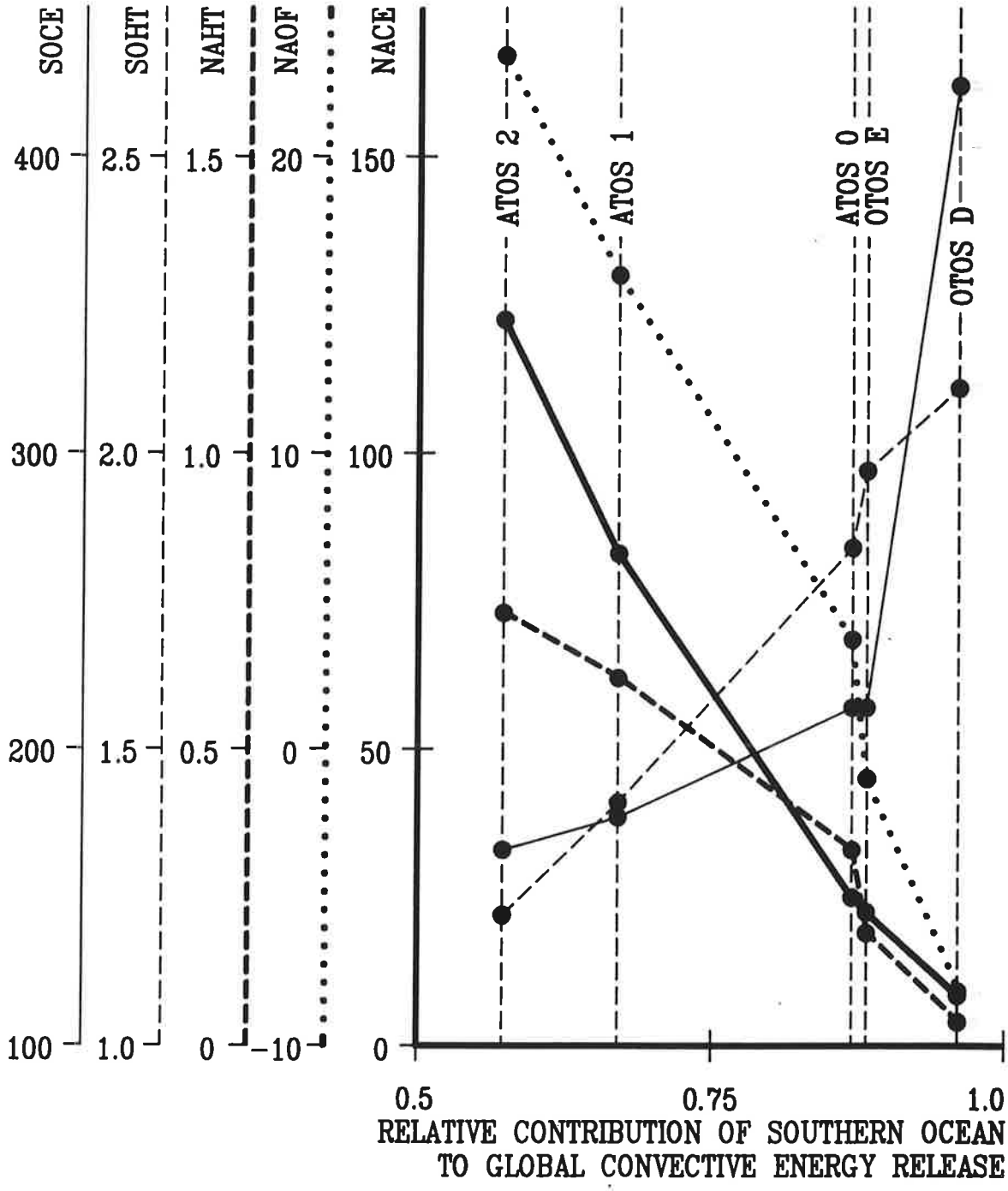

Fig. 17 Circulation indices as a function of fraction of the total potential energy release by convective mixing provided by the Southern Ocean

absolute values, which depend strongly on our rather simple assumption on the isotopic gas transfer velocity. The closest agreement with the observations is found in the standard run ATOS1 (Fig. 16). Experiments OTOSE, OTODS and ATOSø, which have insufficient North Atlantic deep water formation, fail to reproduce the characteristic tongue of young deep water extending southward into the South Atlantic. The differences in the Pacific are less pronounced, but here also the standard run yields the best agreement.

Fig. 17 summarizes the principal differences between the five experiments in terms of six selected circulation indices. The experiments are ordered with respect to the first index, plotted on the abscissa axis, representing the fraction of the total potential energy release by convective mixing which is provided by the Southern Oceans. The remaining five indices, plotted (with five different scales) on the ordinate axis, represent:

(i) The Convective Energy release in the North Atlantic (CENA);

(ii) the Convective Energy release in the Southern Ocean (CESO);

(iii) the meridonal Heat Transport in the North Atlantic at 30°N, the latitude of maximal heat flux (HTNA);

(iv) the southward Heat Transport in the Southern Ocean at 30°S (HTSO);

(v) the North Atlantic OutFlow of deep water across 30°S.

The curves demonstrate the major changes in all six indices brought about by the relatively minor differences in the surface heat flux forcing.

All circulation indices are seen to vary monotonically with the North-South partitioning of the total convective energy release. Following the sequence of the five experiments ATOS2 to OTOSD from left to right, the convective energy release in the North Atlantic decreases continuously, while the convective energy release in the Southern Ocean increases. The deep outflow from the North Atlantic and the Atlantic heat flux both decrease through the sequence, while the total heat flux at

30°S increases.

In essence, the sequence of experiments describes a gradual transition from a deep ocean circulation regime characterized by a strong southward "conveyor-belt type" transport in the Atlantic to a circulation regime in which the deep Atlantic is relatively stagnant and most of the deep water formation occurs in the Antarctic. The changes are brought about by changes in the rate of of deep water formation in high latitudes, which are extremely sensitive to small changes in the air-sea heat exchange. Although the most obvious signatures are seen in the abyssal circulation, significant changes also occur in the climatically important heat fluxes through the air-sea interface, as evidenced by the large relative changes in the meridional heat fluxes in the North Atlantic and, to a smaller extent, in the Southern Ocean.

The changes affect also the uptake of CO_2 by the ocean. The impulse response function describing the response of the atmospheric CO_2 concentration to a δ-function injection of CO_2 into the atmosphere, for example, is characterized by a 50% larger time constant (~ 150 years) for a coupled atmosphere-ocean carbon cycle model based on the standard circulation ATOS1 than the time constant found by Maier-Reimer and Hasselmann (1987) in their original model, which was based on the more rapidly overturning circulation OTOSD.

The sensitivity of the ocean uptake of CO_2 to changes in the ocean circulation, and the sensitivity of the ocean circulation in turn to changes in the atmospheric forcing, imply that computations of climatic change produced by anthropogenic CO_2 emissions should be carried out, if possible, with a fully coupled three-dimensional global ocean - atmosphere - carbon cycle model.

CONCLUSIONS

The principal conclusions of our study may be summerized as follows:

1) An economical global ocean circulation model with $3.5^{\circ} \times 3.5^{\circ}$ horizontal resolution, 11 vertical layers and a time step of 1 month based on large scale geostrophic dynamics is able to reproduce most of the principal observed water mass properties of the global ocean circulation, including salinity, temperature and tracer (eg. $\Delta^{14}C$) distributions and water mass and heat transports.

2) The circulation is very sensitive to small changes in the high latitude heat flux. These can produce large changes in the relative rates of deep water formation in the North Atlantic and Southern Ocean, leading to a transition from the present circulation regime, characterized by a dominant deep water source in the North Atlantic, to a circulation regime, which may have been more typical of previous climate epochs, in which the Antarctic Circumpolar front represents the major deep water source.

3) The sensitivity with respect to the parametrization of the heat flux is consistent with previous findings of the sensitivity of the ocean circulation to changes in the fresh water flux (Maier-Reimer and Mikolajewicz, 1989, Mikolajewicz and Maier-Reimer, 1990).

4) The simulations provide support for the view that at least two equilibrium states of the ocean circulation exist, which are characterized by different rates of deep water formation in the two hemispheres, and that the transition from one circulation regime to another can be brought about by relatively low thresholds of external forcing.

ACKNOWLEDGEMENTS

We thank Dirk Olbers and Jürgen Willebrand, for tireless support and continuous advice over a long period during which the model was developed. We are grateful to Wallace Broecker for enthusiastic encouragement and enlightening criticism during a visit to the

Max-Planck-Institute in a critical phase of the model testing. We thank also Marion Grunert and Heinke Hoeck for their assistance in preparing the figures. The work was supported in part by grants from the climatic programs of the Bundesminister für Forschung und Technologie (grant no. 07kft470) and the Commission of the European Community (grant no. EV4C0035-D)

References:

Arakawa, A. and V.R.Lamb, 1977: Computational design of the basic dynamical Processes of the UCLA General Circulation Model. Meth. Comp. Phys. 17, 173 - 265

Bacastow,R. and E.Maier-Reimer, 1990: Ocean-circulation Model of the Carbon Cycle. Climate Dynamics 4, 95 - 126.

Bainbridge, A.E., 1981: GEOSECS Atlantic expedition, Vol.2, Sections and profiles. US Government Printing Office, Washington DC 20402, Stock No. 038-000-00435-2.

Bakan,S., A.Chlond, U.Cubasch, J.Feichter, H.Graf, H.Grassl, K.Hasselmann, I.Kirchner, M.Latif, E.Roeckner, R.Sausen, U.Schlese, D.Schriever, I.Schult, U.Schumann, F.Sielmann, and W.Welke, 1991: Climate response to smoke from the burning oil wells in Kuweit. Nature, 351, 367 - 371.

Berger,W.H.,1990: The Younger Dryas cold spell - a quest for causes. Paleogeogr., Paleoclim., Palaeoecol. 89, 219-237.

Berger,W.H. and R.S.Keir, 1984: Glacial-holocene changes in atmospheric CO2 and the deep sea record. In: Hansen,J.,E and T.Takahashi (eds): Climate processes and Climate sensitivity.AGU Washington DC, pp.337-351.

Berger, W.H. ans J.S.Killingley 1982: The Worthington effect and the origin of the Younger Dryas. J. Mar. Res. 40, Suppl. 27 - 38.

Broecker,W.S., M.Andree, W.Wolfli, H.Oeschger, G.Bonani,, J.Kennet, and D.Peteet, 1988 : The Chronology of the last Deglaciation: Implications to the Caus of the Younger Dryas Event. Paleoceanogr. 3, 1-19

Bryan,F. 1986: High latitude salinity effects and interhemispheric thermohaline circulations.Nature 305, 301-304.

Bryan,K. 1969: A numerical method for the study of the circulation of the world ocean. J. Comp. Phys. 4 , 347 -376.

Bryan ,K. and L.J.Lewis, 1979: A Water Mass Model of the World Ocean. J. Geoph. Res. 84, 2503 - 2517

Cubasch,U., K.Hasselmann, H.Höck, E.Maier-Reimer, U.Mikolajewicz, B.D.Santer, and R.Sausen 1991: Time dependent Greenhouse warming Computations with a coupled Ocean-Atmosphere model. subm. to Nature.

Gordon, A.L., 1986: Interocean Exchange of Thermocline Water. J. Geoph. Res. 91, C4, 5037 - 5046

Hasselmann, K., 1982: An Ocean Model for Climate Variability Studies. Progr. Oceanogr 11, 69-92.

Heinze,C. and E.Maier-Reimer, 1990: Glacial pCO2 Reduction by the World Ocean - Experiments with the Hamburg Carbon Cycle Model.

Paleoceanography, in press.

Hellerman, S. and M.Rosenstein 1983: Normal monthly windstress over the world ocean with error estimates. J.Phys. Oceanogr. 13, 1093 - 1104.

Jouzel,J., C.Lorius, J.R.Petit, C.Genthon, N.I.Barkov,V.M.Kotlya- kov and V.M.Petrov,1987: Vostok ice core: a continuous isotope temperature record over the last climatic cycle (160,000 years). Nature 329,403-408

Levitus, S. 1982 : Climatological Atlas of the World Ocean. NOAA Prof.Paper No.13. Rockville, Md. 173 pp., 17 fiches.

Maier-Reimer,E. and K.Hasselmann, 1987: Transport and storage of CO2 in the ocean - an inorganic ocean-circulation carbon cycle model. Climate Dynamics 2, 63-90.

Maier-Reimer, E. and U.Mikolajewicz , 1989: Experiments with an OGCM on the cause of the Younger Dryas. In : Proc. JOA 1988, pp 87 - 100.

Maier-Reimer, E. and U.Mikolajewicz , 1990: The Hamburg Large Scale Geostrophic Ocean Circulation Model. Report of the Deutsches KlimaRechenZentrum.

Marotzke,J.,P.Welander, and J.Willebrand 1988: Instability and multiple steady states in a meridional-plane model of the tjermohaline circulation. Tellus 40A, 162-172.

Mikolajewicz, U. and E. Maier-Reimer, 1990: Internal Secular Variability in an OGCM. Climate Dynamics 4,145 - 156.

Mikolajewicz, U., B. Santer and E. Maier-Reimer, 1990: Ocean Response to Greenhouse Warming, Nature 345,589 - 593.

Manabe,S. and R.J.Stouffer,1988: Two stable Equilibria of a coupled Ocean-Atmosphere Model. J.Climate 1, 841 - 866.

Olbers, D.J., M.Wenzel, and J.Willebrand, 1985: The inference of North Atlantic circulation patterns from climatological hydrographic data. Rev.Geoph. 23, 313-356.

Redi,M.H. 1982: Oceanic isopycnal mixing coordinate rotation. J.Phys. Oceanogr. 12, 1154-1158.

Roemmich,D. and C.Wunsch, 1985: Two trans-atlantic sections: Meridional circulation and heat flux in the subtropical North Atlantic Ocean, Deep Sea Res. 32, 619 - 664.

Rooth,C., 1982: Hydrology and ocean circulation. Progr. Oceanogr., 11, 131-149

Sarnthein, M. and R.Tiedemann, 1990: Younger Dryas-Style Cooling Events at Glacial Terminations I-VI ar ODP Site 658: Associated Benthic δ^{13} C Anomalies Constrain Meltwater Hyoithesis. Paleoceanography 5, 1041 - 1055.

Sarmiento, J.L. and K.Bryan, 1982: An ocean transport model for the North Atlantic. J.Geophys. Res., 87, 394 - 408

Stefan, R., 1891 : The Theory of Ice Formation especially in the Arctic Ocean. Ann. Phys. Chem. N.F. 42, 269 - 278.

Stommel, H., 1961: Thermohaline convection with two stable regimes of flow. Tellus 13, 224-230

UNESCO 1981: Tenth report of the joint panel on oceanographic tables and standards. UNESCO technical papers in marine sci. No 36, UNESCO, Paris.

Welander, P., 1986: Thermohaline effects in the ocean circulation and related simple models. In: J.Willebrand and D.L.T.Anderson (eds): Large_scale Transport Processes in Ocean and Atmosphere, pp. 163 -200, Reidel publ.

Wüst, G., 1933: Schichtung und Zirkulation des Atlantischen Ozeans. Das Bodenwasser und die Gliederung der Atlantischen Tiefsee. In: Wissenschaftliche Ergebnisse der Deutschen Atlantischen Expedition auf dem Forschungs- und Vermessungsschiff "Meteor" 1925 - 1927, 6, 106pp.

Appendix 1: Decomposition into modes

For simplicity we neglect in this section the deviations from a uniformly rotating plane. The linearized equations of inviscid motion in the f-plane are

$$(\partial_t u_{ik} + f\ \varepsilon_{ij} u_{jk}\ ) + \partial_i p_k = 0, \qquad \text{(A1.1)}$$

where u_{ik} are the horizontal components of velocity at level k, f is the Coriolis parameter, p_k is the pressure normalized by ρ_{0k}, the reference density of layer k according to the Boussinesq approximation, and ε_{ij} is the antisymmetric tensor. The number of layers is N.

The hydrostatic approximation yields the pressure

$$p(z) = g\rho_{00}\zeta + \int_z^0 g\rho(s)ds \qquad \text{(A1.2)}$$

A density anomaly $\delta\rho$ at depth D contributes $g\ \delta\rho(B - D)/B$ to the forcing of the barotropic motion, $+ g\ \delta\rho\ D/B$ to all baroclinic motion below D and $-g\ \delta\rho(B - D)/B$ to the baroclinic motion above D.

For the formulation of the implicit time discretization we perform the transformation

$$V_1 = \sum_{k=1}^{N} \Delta z_k u_k,$$

and

$$V_k = H_k\ (\ u_k - u_{k-1}\ ) k = 2, \ldots, N,$$

where $H_k = D_k\ (B - D_k)/\ B$, and $D_k = \sum_{n=1}^{k-1} \Delta z_n$ $(D_1 = 0)$ corresponds to the reduced depth of a two layer mode defined at the depth D_k.

The inverse transformation is given by

$$u = \sum_{n=k}^{N} V_k\ /(B - D_k) - \sum_{n=1}^{k-1} V_k\ /\ D_k + \hat{u}$$

The layer thickness Δz_k is normally defined by the computation levels. However, at locations where the assumed topography intersects the levels

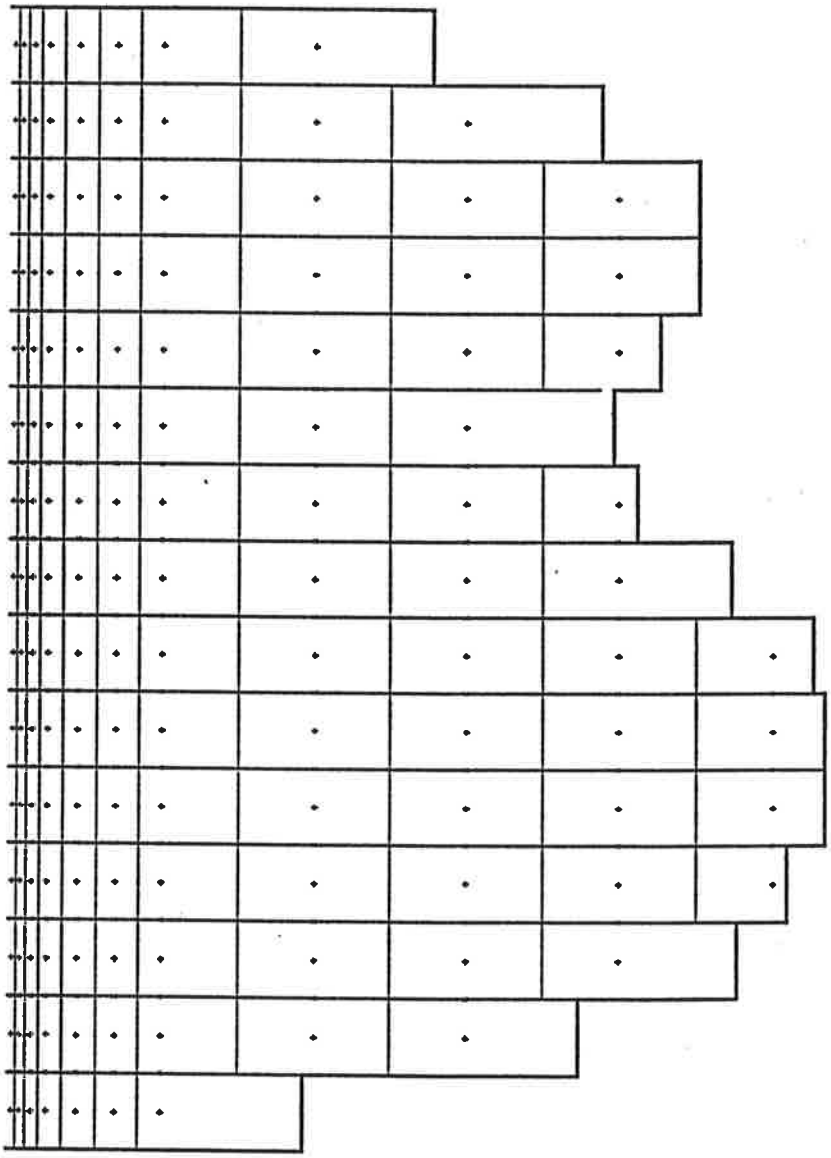

Fig.A1 Position of grid points on 30^{o} N in the Atlantic

of computation, a modified layer thickness is introduced in order to obtain smoother variations of depth than could otherwise be achieved for the low number of levels of our model. Fig.A1 shows the models resolution in the Northern Atlantic at 30 deg N.

V_1 is the barotropic mode, while for $k > 1$ V_k represent the N-1 computational baroclinic modes of the model grid. They are driven by the vertical shear of the horizontal pressure gradients, i.e. the local density gradients. Each of the baroclinic modes represents a flow field with vanishing $\int u dz$.

For the time discretization, the modes are treated separately. For each mode $k \geq 2$ the convergence $W_k = \partial_i V_{ik}$ creates a profile of vertical velocity at levels m:

$$w = 0 \qquad \text{at the bottom}$$

$$w_{km} = W_k (D - D_m)/(D - D_{k-1}) \quad \text{for } D_m > D_{k-1} \qquad \text{A1.3}$$

$$w_{km} = W_k D_m / D_{k-1} \quad \text{for } D_m < D_{k-1}$$

(For k=1, w at the surface is the rate of change of sea level). The vertical velocity profiles w_{kl} with $k \neq 1$ provide the coupling between the different modes with a one time step delay.

The decoupled mode equations can be written:

$$\partial_t V_i + f \varepsilon_{ij} V_j + \partial_i p = F \qquad \text{A1.4}$$

$$\partial_t p + c^2 \partial_i V_i = 0 . \qquad \text{A1.5}$$

where the phase velocity c is determined by the overall stratification, but with the strongest contribution coming from the level associated with the mode under consideration (including the air-sea difference of density for the barotropic mode).

For the experiments described in this paper, we applied rigorously the Euler backward procedure, in which the time discretization $\partial_t (V,p) = \tau^{-1}((V,p)^t - (V,p)^{t-\tau})$ links the variables at t. Insertion of A1.5 and

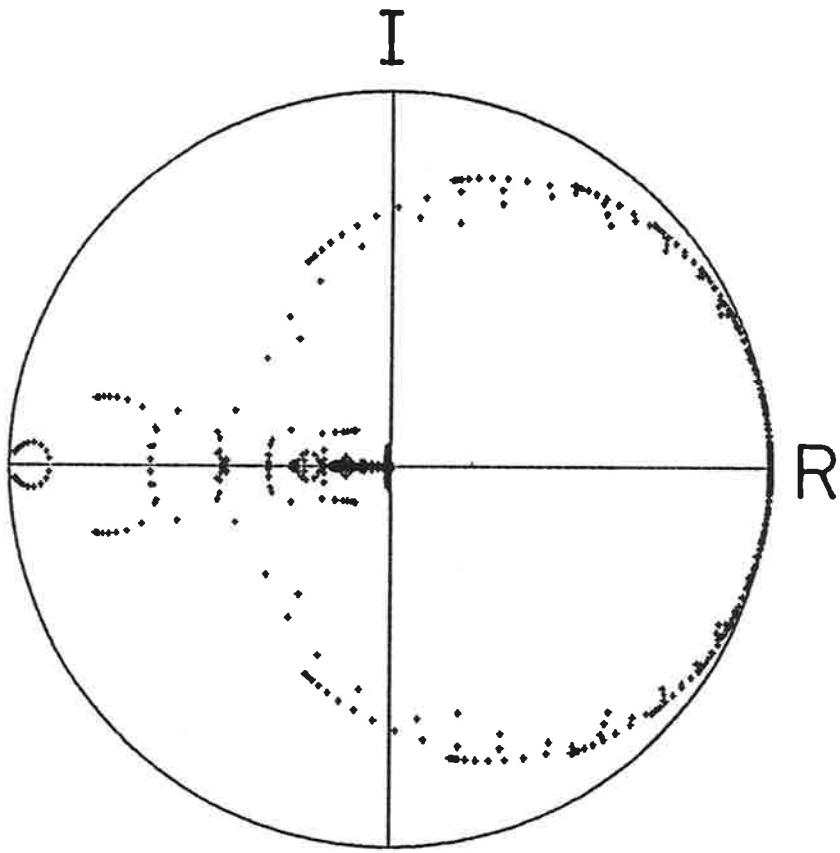

Fig. A2 Location of the eigenvalues in the complex plain of the Euler backward scheme for gravity wave phase speed c= 1m/s, Δx= 500 km and Δt = 30d.

A1.3 into A1.4 yields

$$\partial_t V_{ik} + H_k f \varepsilon_{ij} V_{jk} + (g/\rho_{0k})\partial_i F'_k = 0,$$

with $F' = D'_k \rho_k + \tau \sum D'_l w_{kl}(\rho_k - \rho_{k-1})$. Replacing all abbreviations by their definitions, we obtain finally an elliptic system of the form:

$$\tau^{-1}V_1 - f V_2 - \tau c^2(\partial_{11} V_1 + \partial_{12} V_2) = F_1$$

$$\tau^{-1}V_2 + f V_1 - \tau c^2(\partial_{22} V_2 + \partial_{12} V_1) = F_2 , \qquad \text{A1.6}$$

where F contains the density field at the beginning of the timestep, frictional forces, and the windstress for the barotropic and the first baroclinic mode.

For the baroclinic modes the system is solved by iteration. Because of the error damping associated with the discretization, there is no need for very high accuracy; the iteration is stopped after 12 sweeps, which reduce the error of the first guess (the values of the preceding time step) to approximately 5 % .

For the barotropic mode the convergence is very slow, so that the equations are solved directly by elimination. The matrix is triangularised once for the initial stratification. As the matrix is sparse, there is no need for pivoting. The matrix retains the band structure in the triangularisation. The triangularized band matrix enables a rather efficient solution of A1.6 at each time step of the integration.

Appendix 2: Wave dispersion

For each mode the implicit discretization can be written formally as the simplified system:

$$u^t - f \tau v^t + \partial_x p^t \tau = u^{t-\tau}$$

$$v^t + f \tau u^t + \partial_y p^t \tau = v^{t-\tau}$$

$$p^t + c^2 \tau (\partial_x u^t + \partial_y v^t) = p^{t-\tau}.$$

Outside the equatorial belt, $f\tau >> 1$ and we can neglect the momentum

acceleration. Then

$$p^t = p^{t-\tau} - \tau\, c^2 (u_x + v_y), \text{ with } v = p_x^t / f \text{ and } u = - p_y^t / f.$$

For any wavelike disturbance $p^{t-\tau} = P_0 \exp(i(kx + my))$ we have

$$p^t = P_0 \exp(i(kx+my))/(1 + \beta\, ik\, \tau\, c^2 / f^2),$$

which, for small c, is a good approximation for the exact expression $p^{t-\tau}\exp(-i\ \beta\ k\ c^2\tau/f^2)$, valid for waves whose wavelength is large compared with the Rossby radius of deformation.

Near the equator this approximation is not valid. We performed the eigenvalue analysis for a wavelike disturbance exp(ikx) for all variables in an equatorial channel with 12 gridpoints on each side of the equator. Fig. A2 shows the location of the eigenvalues in the complex plane for the the space and time steps of our model for a typical phase speed of 2 m/s for the gravity wave. The cluster in the center of the circle represents the highly damped gravity waves, while the many eigenvalues with modulus of almost unity represent the only weakly damped Rossby waves.

Appendix 3: Numerical diffusion of the upwind scheme.

The advection of temperature and salinity is formulated in an implicit upwind scheme:

$$T^t = T^{t-\tau} + \tau \sum u_i^+ (T_i^t - T^t) \quad ,$$

where the summation runs over all neighbouring points for which u_i is directed towards the point of computation. For the suppression of mode splitting we add an explicit diffusion of 200 m^2/s. It can be easily shown (cf. Bacastow and Maier-Reimer, 1990) that the upwind scheme can be decomposed into a sum of advective and diffusive flux divergence with diffusion coefficients $|u|\ \delta x$.

In a onedimensional constant flow u, a wavelike disturbance $T^{t-\tau} = T_0 \exp(ikx)$ is modified by this scheme according to

$$T^t = T_0 \{ 1 + (u\tau/\delta x)\ [1-\cos(k\ \delta x) + i\sin(k\ \delta x)]\}^{-1} \exp(ikx) \ .$$

This represents in addition to the phase shift a damping similar to that produced by a diffusivity in the order of $|u|\ \delta x$. Many schemes have been presented to overcome this damping. In most cases, the different schemes

are intercompared for the situation of a uniformly rotating fluid. Russell and Lerner (1981), however, have shown in their presentation of the "slope" scheme that in a practical application the diffusivity of the upwind scheme appears to be less detrimental than would be concluded from such simplified tests.

To investigate the effective diffusivity in our model, we performed some simple experiments with an assumed δ-function-like initial distribution (the worst case) of an artificial tracer:

1) The initial distribution of an artificial tracer was set at 10^6 at a point off China in both of the overlapping grids. The transport was computed in the same way as temperature and salinity in the model. This location was chosen to avoid as far as possible regions of convective mixing. The computation was performed for 10 years.

2) Exp.1 was repeated with the amplitude of the numerical diffusive terms doubled..

3) 1000 tracer particles were distributed over an area represented by two gridpoints. The trajectories were computed with a one day time step. A diffusion coefficient of 200 m^2/s (same as the explicit diffusion in the circulation model for the suppression of mode splitting) was simulated in this run by the superposition of Brownian motion of appropriate amplitude on the advection field.This experiment with small explicit diffusivity demonstrates the effect of shear dispersion on an initial gridelement.

4) Exp. 3 was repeated with an (acceptable) explicit horizontal diffusion coefficient of 10^3 m^2/s and a vertical diffusion coefficient of 10^{-4} m^2/s.

Fig. A3 shows Pacific sections for the experiments 1) and 2). During the 10 years of computation, the tracer is seen to remain almost entirely above the main thermocline. The doubled diffusion coefficient creates some visible but non-substantial additional dilution.

Fig A4 shows the time development of the horizontal and vertical variance for the four experiments. Most of the apparent diffusion of exp.1 is clearly explained by shear diffusion, not by numerical diffusion.

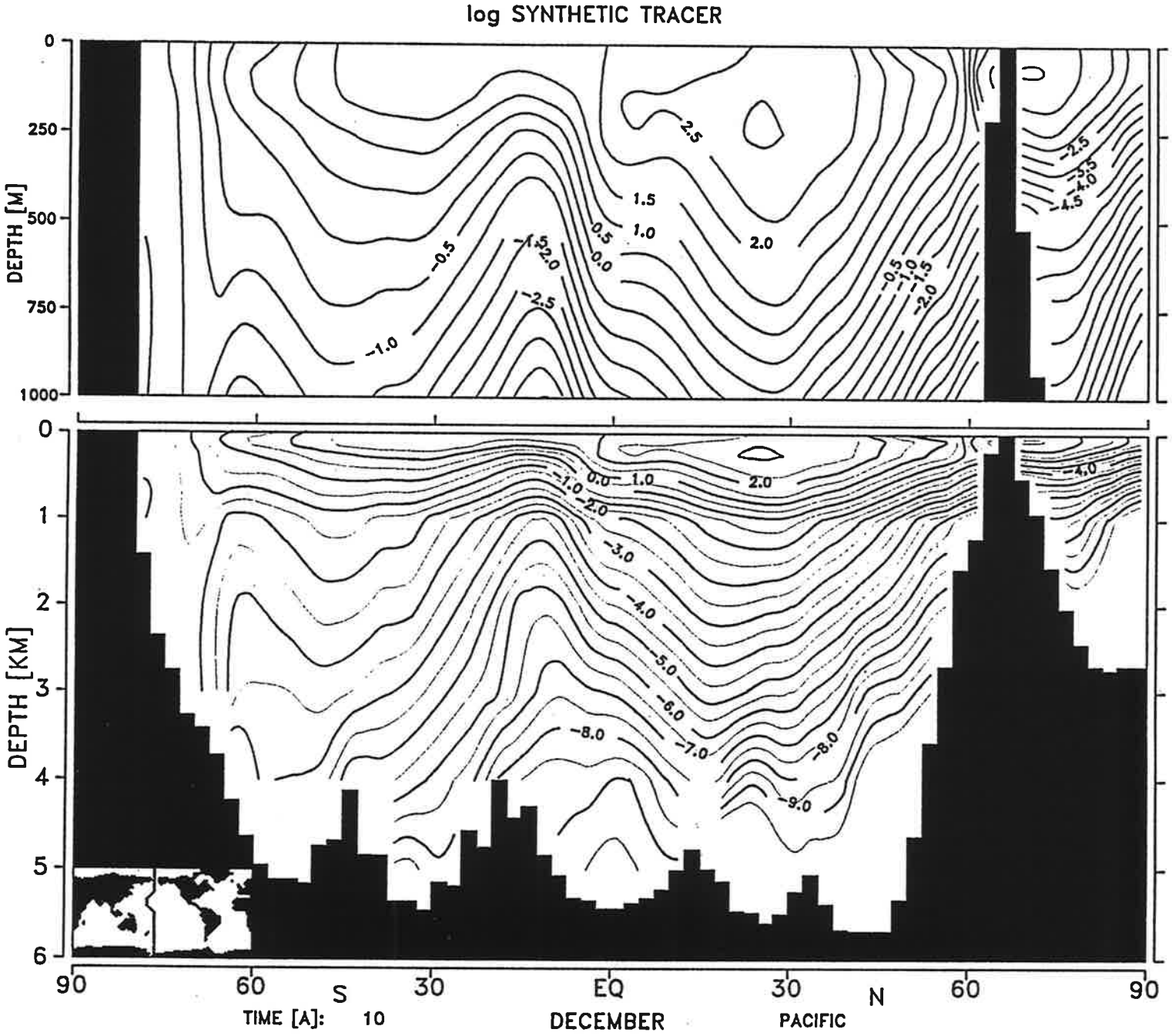

Fig. A3a Pacific sections of an artificial dye release of 10^6 units at a point off China after 10 years with standard advection

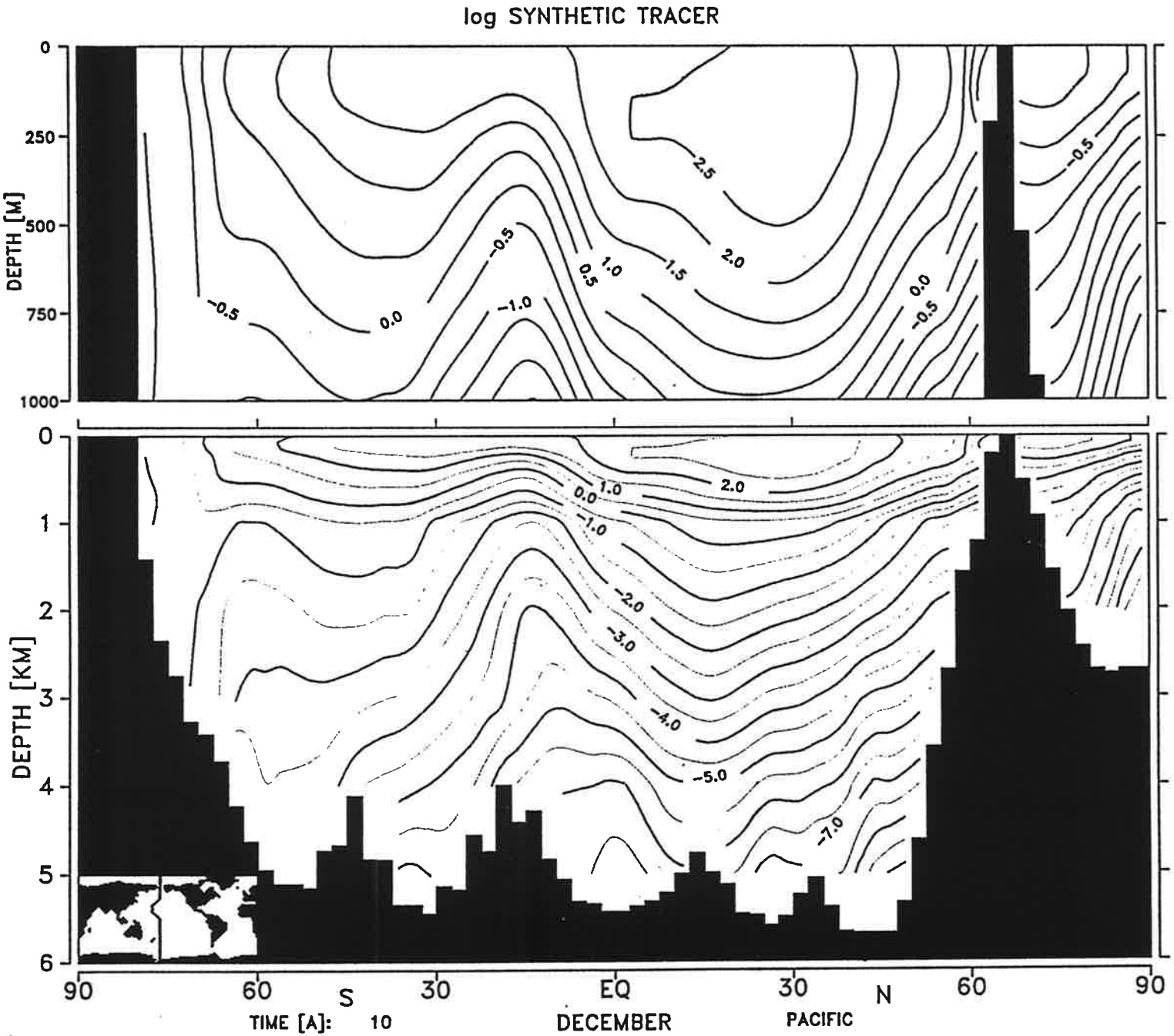

Fig. A3b Pacific sections of an artificial dye release of 10^6 units at a point off China after 10 years with standard advection with doubled numerical diffusion

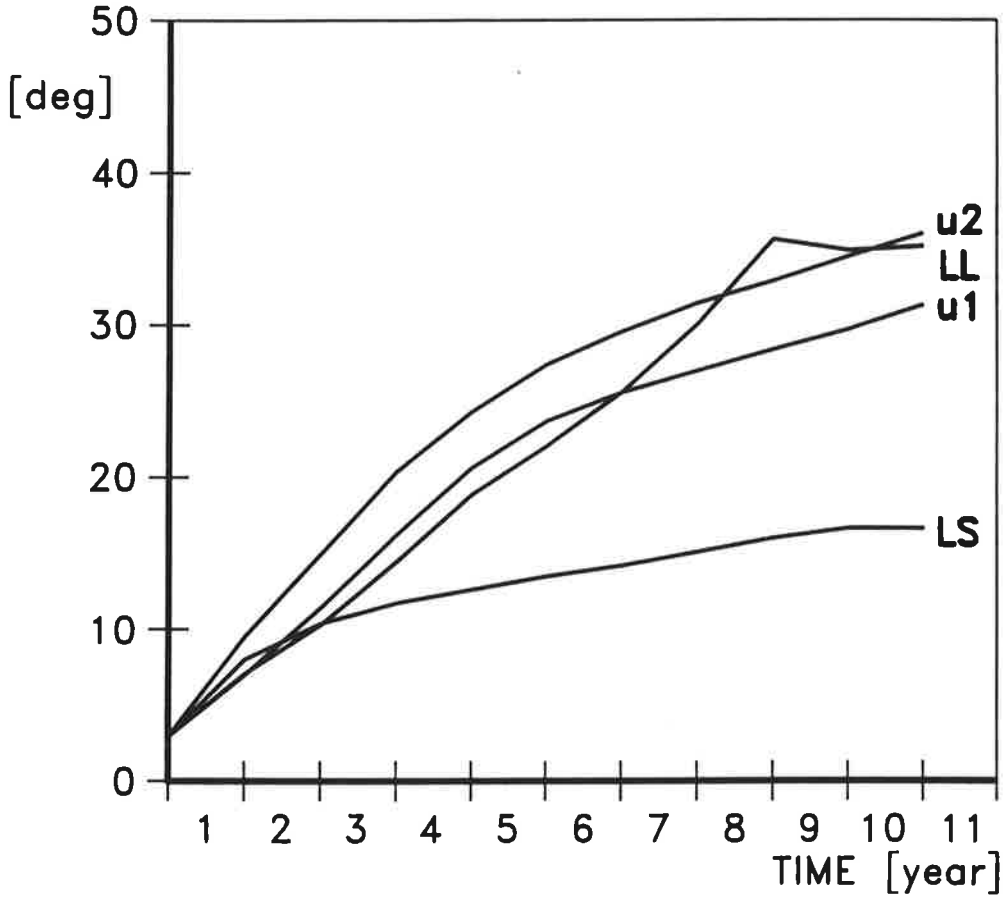

Fig. A4a Horizontal spreading of an artificial dye release off China
U1) standard upwind advection
U2) upwind advection with doubled numerical diffusion
LS) tracer particles with explicit horizontal diffusion coefficient of 200 m^2/s.
LL) tracer particles with explicit horizontal diffusion coefficient of 1000 m^2/s and a vertical diffusion coefficient of 10^{-4} m^2/s.

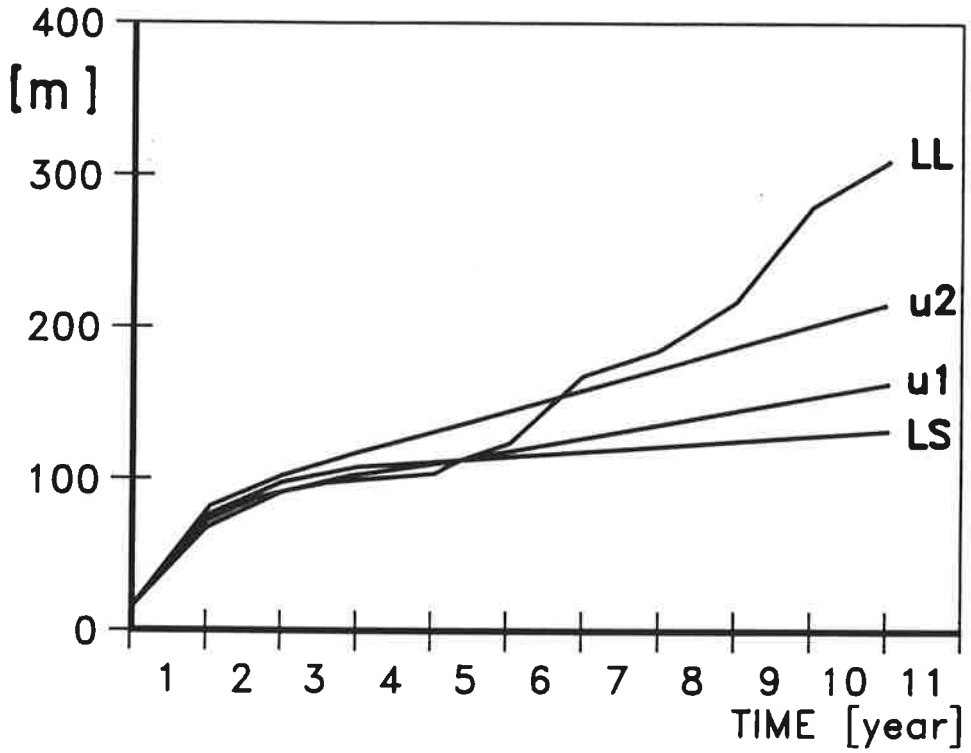

Fig. A4b Vertical spreading of an artificial dye release off China
U1) standard upwind advection
U2) upwind advection with doubled numerical diffusion
LS) tracer particles with explicit horizontal diffusion coefficient of 200 m^2/s.
LL) tracer particles with explicit horizontal diffusion coefficient of 1000 m^2/s and a vertical diffusion coefficient of 10^{-4} m^2/s.